

From biomass to battery: lignin-derived carbons achieving unprecedented high capacity retention in potassium batteries

Original

From biomass to battery: lignin-derived carbons achieving unprecedented high capacity retention in potassium batteries / Benigno, A.; Raviolo, S.; Trano, S.; Domenici, S.; Castellino, M.; Francia, C.; Gaspar, D.; Pereira, L.; Bella, F.. - In: CHEMICAL ENGINEERING JOURNAL. - ISSN 1385-8947. - ELETTRONICO. - 528:(2026), pp. 1-15. [10.1016/j.cej.2025.172142]

Availability:

This version is available at: 11583/3008318 since: 2026-03-06T10:17:04Z

Publisher:

Elsevier

Published

DOI:10.1016/j.cej.2025.172142

Terms of use:

This article is made available under terms and conditions as specified in the corresponding bibliographic description in the repository

Publisher copyright

(Article begins on next page)



From biomass to battery: lignin-derived carbons achieving unprecedented high capacity retention in potassium batteries

Antonio Benigno^a, Sofia Raviolo^a, Sabrina Trano^a, Sara Domenici^a, Micaela Castellino^{a,b}, Carlotta Francia^a, Diana Gaspar^d, Luís Pereira^{c,d,*}, Federico Bella^{a,*}

^a Department of Applied Science and Technology, Politecnico di Torino, Corso Duca degli Abruzzi 24, 10129, Torino, Italy

^b Center for Sustainable Future Technologies @Polito, Istituto Italiano di Tecnologia, Via Livorno 60, 10144, Torino, Italy

^c AlmaScience Colab, Madan Parque, 2829-516, Caparica, Portugal

^d CENIMAT|i3N, Department of Materials Science, School of Science and Technology, NOVA University Lisbon and CEMOP/UNINOVA, Campus da Caparica, 2829-516, Caparica, Portugal

ARTICLE INFO

Keywords:

Hard carbon
Potassium-ion battery
Anode
Biomass
Lignin

ABSTRACT

The increasing demand for sustainable energy storage solutions has led to a growing interest in post-lithium-ion battery technologies. In this context, potassium-ion batteries (KIBs) have emerged as a promising alternative for large-scale applications due to the high natural abundance, cost-effectiveness, and favorable electrochemical properties of potassium. Hard carbon materials derived from biomass are particularly attractive as KIB anodes, offering a sustainable solution with appropriate structural and electrochemical behavior. This study investigates the electrochemical performance of hard carbons derived from lignin-rich biomass residues, which are chemically activated with different KOH ratios. Structural, morphological, and compositional analyses are conducted to elucidate the influence of activation parameters on porosity, chemical composition, graphitization degree, and interlayer spacing. Additionally, chemical composition and formation mechanism of the solid electrolyte interphase layer are in-depth analyzed. This work underscores the potential of biomass-derived hard carbons as sustainable anode materials for next-generation KIBs, aligning with circular economy principles and renewable energy storage strategies, and also targeting unprecedented electrochemical performances in terms of device durability.

1. Introduction

The effects of climate change are no longer a distant threat; instead, they are manifesting with unprecedented frequency and severity in our daily lives [1]. Hence, the need to accelerate the energy transition to address and mitigate this issue has become more pressing than ever. Batteries as electrochemical storage systems are crucial to address the intermittency related to renewable energy sources [2]. Particularly, lithium-ion batteries (LIBs) have been highly commercialized for different kinds of applications, such as hybrid electric vehicles, stationary energy storage, and portable electronic devices, thanks to their long cycle life and high energy density [3].

The scarcity and uneven distribution of lithium [4,5] raise significant concerns about the long-term viability of Li-based energy storage in meeting the global storage demand [2]. To address this challenge and promote more sustainable solutions, research is increasingly focusing on

the development of alternative post-lithium technologies, particularly for applications that do not require high energy densities [6]. In this scenario, potassium-ion batteries (KIBs) have gained attention as a greener and cost-effective option for large-scale stationary energy storage [7]. Since the first prototype, developed in 2004 [8], the number of related publications exponentially increased [9]. Unlike lithium, potassium is one of the most abundant elements in the Earth crust, and it is homogeneously distributed [10]; consequently, the corresponding carbonate price is one order of magnitude lower than that of lithium [11].

Further advantages make potassium competitive among the other alkali-metals. In first place, its standard electrode potential (−2.93 V vs. standard hydrogen electrode) is the closest to lithium one (−3.04 V), promising high operational voltages and high energy densities [12]. Potassium even exhibits a lower standard electrode potential in carbonate solvents, compared to lithium [13]. Moreover, despite K-ion larger radius, its Stokes' radius results in being smaller than that of both

* Corresponding authors.

E-mail addresses: lmnp@fct.unl.pt (L. Pereira), federico.bella@polito.it (F. Bella).

<https://doi.org/10.1016/j.cej.2025.172142>

Received 3 September 2025; Received in revised form 20 November 2025; Accepted 20 December 2025

Available online 23 December 2025

1385-8947/© 2025 The Authors. Published by Elsevier B.V. This is an open access article under the CC BY license (<http://creativecommons.org/licenses/by/4.0/>).

lithium and sodium, ensuring a high ionic diffusion rate in aqueous and non-aqueous electrolytes [13]. Finally, contrary to lithium, potassium does not form an alloy with aluminum at low voltages, thus the latter can be used as a current collector instead of copper, bringing down the production costs and the overall cell weight. Nevertheless, KIBs still face several hurdles that hinder their full development [7].

Potassium-ion large size represents a significant challenge in designing stable and high performance electrodes. The scientific community is working on electrodes capable of accommodating K-ions while minimizing volume expansion, which can cause structural deformation and poor cycling stability [14]. For example, commercial graphite, which is the most common anode material in LIBs, can store K-ions through intercalation/de-intercalation processes. However, its inter-layer distance is not adequate for accommodating K-ions, leading to a substantial volume expansion (*i.e.*, 161% of the initial volume), which results in poor cycling performance [15,16]. To overcome these challenges, various materials have been explored as promising anode candidates, including alloys [15], MXenes [17], conversion materials [18], organic materials [19], and amorphous carbons [20]. Among these, amorphous carbon materials – particularly hard carbons (HCs) [21–23] – are the most widely studied due to their low cost, high availability, and tunable properties [24].

HC materials consist of randomly oriented graphene layers organized by short-range stacks, spaced enough to accommodate K-ions during intercalation and deintercalation.

Besides the intercalation diffusion-controlled mechanism, K^+ ions can also exploit a pseudo-capacitive, adsorption surface-controlled mechanism in HCs. Owing to their amorphous structure, these materials possess a high specific surface area and are abundant in pores, edges, and defects. These characteristics, together with the presence of numerous oxygen-containing functional groups, collectively provide additional active sites for K^+ ion adsorption, thereby enhancing electrochemical performance without significantly altering the electrode structure [25,26]. This surface-controlled mechanism is less invasive because ions primarily interact with the electrode surface rather than diffusing into the bulk material, reducing the likelihood of structural damage and capacity degradation during cycling. Furthermore, this mechanism facilitates faster ion transport compared to conventional intercalation processes [27,28]. This discussion will be further elaborated in the dedicated Section 3.3.

Porous materials exhibit a range of pore sizes, each playing a distinct and complementary role in electrochemical energy storage. In particular, micropores play a significant role by serving as active sites for potassium-ion storage. They also function as ion-buffering reservoirs, which help accommodating volume changes during cycling and thereby maintaining structural integrity and improving specific capacity [29]. Meanwhile, mesopores significantly contribute by forming interconnected channels that facilitate the diffusion of ions and the penetration of electrolytes [30].

HCs are widely used as anode materials also in sodium-ion batteries (SIBs) [31]. Similar to potassium, sodium suffers from electrode volume expansion due to its larger ionic radius compared to lithium. Therefore, the amorphous architecture of HCs is beneficial for SIBs anodes, as it can better accommodate the volume changes during ion insertion and extraction [32].

Indeed, HCs used in both KIBs and SIBs share similar structural features, including large interlayer spacing, high surface area, and well-developed porosity, which are beneficial for maintaining structural integrity during cycling and enhancing the overall capacity. The crucial difference lies in the tuning of the pore structure, which is strongly influenced by the distinct ion storage mechanisms proposed for the two systems. In SIBs, a pore-filling mechanism is generally reported, making mesopores highly beneficial as they facilitate the insertion of sodium ions while preserving the electrode structure. Conversely, in KIBs, HCs primarily rely on ion adsorption processes, where microporosity plays a more significant role in enhancing storage performance, while pore-

filling is rarely reported [33,34].

One crucial method to tune porosity and the graphitization degree is the activation process, which can be achieved through physical methods, such as CO_2 [35] or steam [36] fluxing, or chemical treatments involving porogen activators. One of these chemical activators is potassium hydroxide (KOH), the addition of which is a conventional and efficient approach to induce porosity and increase the specific surface area [37]. KOH-activation of carbon offers several advantages over other common activating agents, including higher production yield, increased surface area, and well connected porous structures [38]. HCs can be derived from biomass *via* pyrolysis, taking advantage of abundant and renewable resources [39]. Notably, industrial and agricultural wastes can be effectively exploited as biomass precursors, aligning the development of electrode materials with the principles of sustainability and circular economy, rather than relying on petroleum-derived alternatives.

Among all biomass precursors, lignin emerges as a particularly promising candidate for developing HC anodes for both KIBs [40–44] and SIBs [45,46]. This widely available industrial by-product mainly originates from the paper and pulp industries and sawdust residues [47], and exhibits a high carbon yield after pyrolysis [48]. Furthermore, the intrinsic aromatic structure of lignin favors the formation of disordered graphitic domains after carbonization [48]. Lignin is a polymer composed of phenylpropane units containing three different aromatic ring substitution patterns: *p*-hydroxyphenyl (H units), guaiacyl (G units), and syringyl (S units), depending on the wood species. Softwoods (SW) contain a greater proportion of G units and smaller amounts of H units, whereas hardwoods (HW) consist mainly of G and S units [49,50]. These intrinsic differences in lignin composition can strongly influence the structure of the resulting HCs. In particular, SW-derived carbons are reported to exhibit a more amorphous structure [51], which can enhance electrode performance in KIBs by providing a larger number of active sites and facilitating ion transport.

HC production can be integrated with biomass pyrolysis processes for bio-oil generation, further improving resource efficiency. This integration not only enhances the sustainability of the overall process, but—together with the large availability of lignin feedstocks—also makes the production of lignin-derived HCs potentially scalable for industrial applications [52].

This study investigates the potential of HCs obtained from two different lignin-rich biomass residues, activated with various amounts of KOH, as anode materials for KIBs. To evaluate their electrochemical performance and elucidate their behavior, extensive physicochemical, morphological, and electrochemical characterizations were carried out on the carbon powders, as well as on both pristine and cycled electrodes. Unlike most existing studies (also cited in this work) where lignin-derived carbons are typically combined with conductive additives such as Super P or acetylene black to fabricate composite electrodes, our electrodes are prepared without any conductive additive. This additive-free configuration emphasizes the intrinsic conductivity and structural efficiency of the synthesized carbons. Moreover, the materials developed in this work exhibit a highly microporous architecture that provides abundant active sites for K^+ storage. This structural feature plays a key role in the enhanced cycling stability and capacity retention, observed in our electrodes. To the best of our knowledge, the electrodes presented in this work demonstrate capacity retention superior to other lignin-derived activated carbons reported in the lab scale KIB prototype literature [40].

2. Experimental section

2.1. Biocarbons synthesis

Four powder materials were obtained through the pyrolysis and activation of two different lignin-based bio-residues derived from SW and HW. As the SW source, raw Kraft lignin obtained from pine was

used, whereas HW is a Kraft lignin isolated through LignoBoost® process. Each bio-residue was soaked in an aqueous KOH solution (5 M) using different proportions of activating agent to lignin source, namely 2:1 and 1:1. The samples were then kept at 90 °C for 12 h to evaporate the solvent. The mixtures were pyrolyzed for 1 h at 750 °C under a nitrogen-rich atmosphere. After the pyrolysis, the powders were washed several times with distilled water to remove ashes and excess of activating agent. The samples were subjected to several centrifugation cycles (10 min each) at 6000 rpm in deionized water until the pH reached that of the water. Afterwards, the biocarbons were dried overnight at 100 °C. The obtained samples were labelled as SW11, SW21, HW11, and HW21 to indicate the lignin source and KOH ratio, respectively. The resulting powders underwent a ball milling process to enhance particle size homogeneity [53]. The milling was carried out using a Retsch MM400, with the following parameters: 3 cycles at 15 Hz for 20 min each, followed by 2 cycles at 30 Hz of 10 min each. A 15 min rest period was implemented between each cycle to prevent localized overheating.

2.2. Materials characterization

The morphologies of the different biocarbons were characterized by a field emission scanning electron microscope (FESEM) Zeiss SUPRA TM 40 with Gemini column. Acquisitions were made at an acceleration voltage of 5 kV. Energy-dispersive X-rays spectroscopy (EDS) mapping was carried out to evaluate the homogeneity of elemental distribution in the HC samples, using a Zeiss LEO 1530 Gemini microscope.

The Raman spectra were collected in a Renishaw InVia spectrometer using a laser wavelength of 514 nm over a range from 800 to 2200 cm^{-1} . Composition and crystal structure were investigated by X-rays diffraction (XRD) patterns, which were collected using a Bragg-Brentano geometry configuration from 10° and 90°, with a counting time of 140 s per step and 0.02° step size, using a PANalytical X'Pert (Cu K α radiation, $\lambda = 0.154$ nm) diffractometer with a 2D solid state detector (PIXcel). The textural characterization was carried out by measuring the nitrogen adsorption-desorption isotherms at 77 K via a Micromeritics ASAP2010. The specific surface area was determined by the Brunauer-Emmett-Teller (BET) equation [54]. The total pore volume was obtained by Gurvich's rule at a relative pressure of 0.98 [55]. Micropore volume and mesopore area were calculated by using α -plot method (with NPC standard isotherm). The pore size distributions (PSD) of the samples were determined by the quenched-solid density functional theory method for slit/cylindrical pores in the adsorption branch. X-rays photoelectron spectroscopy (XPS) measurements were carried out using a PHI 5000 Versaprobe spectrometer (Physical Electronics, Chanhassen) equipped with a monochromated Al K-alpha source (1486.6 eV). To compensate for the non-conductive surfaces of the sample, a double charge compensation system was used, consisting of an electron beam and Ar^+ . Both survey and high-resolution (HR) scans were acquired using a circular spot with a 100 μm -diameter. HR spectra deconvolution was performed with Multipak version 9.0 software, utilizing the Shirley function for signal background subtraction and pseudo-Voigt curves for fitting photoelectron peaks. The binding energy scale was calibrated using the C 1s peak, setting the C—C component at 284.8 eV as a reference.

2.3. Electrochemical characterization

Milled biocarbon powder (80 wt%) was mixed with polyvinylidene difluoride (PVDF, 20 wt%), to serve as a binder, and *N*-methyl-2-pyrrolidone as a solvent. The resulting mixture underwent a final ball milling step at 30 Hz for 15 min. The obtained slurries were coated onto copper foils using a doctor blade at a wet thickness of 150 μm . Subsequently, the solvent was evaporated in an oven for 90 min at 45 °C. The electrodes were cut into disks of 15 mm and dried under vacuum in a Büchi oven at 120 °C for 4 h. The active mass areal loading of the electrodes was measured to be approximately $(1.99 \pm 0.07) \times 10^{-2}$ mg

cm^{-2} ; the electrode density was found to be $(8.1 \pm 0.2) \times 10^{-4}$ g cm^{-3} , while the dry film thickness was determined to be $(3.08 \pm 0.04) \times 10^{-2}$ mm.

The cells were assembled inside an argon-filled glove box (MBRAUN MB10 compact, $\text{O}_2 < 0.5$ ppm and $\text{H}_2\text{O} < 0.5$ ppm), in half-cell configuration, in both coin cell (LIR2032) and ELCELL (ECC-Std) architectures. Metallic potassium (Merck) served as both counter and reference electrodes, while Whatman glass fiber disks were used as separators. The electrolyte employed in this work was a solution of bis (fluorosulfonyl)imide (KFSI) 1 M dissolved in a 1:1 (v:v) mixture of ethylene carbonate (EC) and diethyl carbonate (DEC).

The cells performance was tested through galvanostatic cycling, that was conducted on an Arbin LBT-21084 battery tester. The cells were subjected to a constant current density of 0.05 A g^{-1} for the long cycling performance test. For the evaluation of their rate performance, after 20 cycles of activation at 0.05 A g^{-1} , the current density was increased (*i.e.*, 0.1, 0.2, 0.4, 0.8, 1, 0.1, 0.05 A g^{-1}) every 10 cycles for each value. Cyclic voltammetry (CV) and electrochemical impedance spectroscopy (EIS) were carried out using a VSP-3e Biologic potentiostat. CV measurements were performed at a constant scan rate of 0.1 mV s^{-1} , while variable-scan CVs (VSCVs) were carried out at increasing scan rates (*i.e.*, 0.1, 0.2, 0.5, and 1 mV s^{-1}). Five initial formation cycles at 0.1 mV s^{-1} were completed before increasing the scan rate. A galvanostatic intermittent titration technique (GITT) was carried out using Arbin instrument: prior to five activation cycles at 0.05 A g^{-1} , several discharging pulses of 15 min each at 0.025 A g^{-1} were followed by 45 min of rest, up to the cut-off voltage of 0.01 V. Once the discharge process was completed, the same protocol was applied for the charge phase, with a positive current up to 3 V. EIS measurements were performed in the frequency range from 100 kHz to 10 mHz, with a potential amplitude of 10 mV. All measurements were taken within a potential window from 0.01 to 3 V. The EIS spectra were fitted using BT-Lab software according to the equivalent circuit model. The fitting procedure employed a Randomize + Simplex algorithm, with a maximum of 5000 iterations for both the randomization and optimization steps. The impedance modulus ($|Z|$) was used as the weighting factor to ensure balanced fitting accuracy over the entire frequency range.

3. Results and discussion

3.1. Materials characterization

As the structure and the surface composition of the samples are deeply influenced by chemical activation with KOH, it is relevant to briefly describe the proposed mechanism involved during this process. Since the lignin used in the activation comes from biomass sources, it is expected that they are rich in oxygen-containing species such as C—O, C = O, —COOH, O—C = O, and —OH. According to the literature [56], the activating agent KOH etches carbon fragments and readily reacts with the O-groups of the biomass, generating a large number of vacancies. These vacancies can be occupied by OH^- anions provided by KOH, leading to the formation of new oxygen-containing groups. Thus, at the end of the process, the density of O-groups in the biochar is expected to be modified and increased relative to that of the non-activated material. Oxygen-containing functional groups play a crucial role in enhancing the electrochemical performance of carbon-based electrodes. These groups serve as active sites for ion adsorption on the surface, thereby improving the capacitive storage mechanism [57]. Additionally, the introduction of oxygen functionalities contributes to the expansion of interlayer spacing in the disordered structure of HC materials [58]. Besides the increment of the number of O-groups, KOH activation also promotes the pore area growth. Indeed, KOH can react with the carbonaceous structure. These reactions release gaseous products (*i.e.*, H_2 , CO, CO_2 , and CH_4), which, while leaving the carbon backbone, form pores within the biochar. Additionally, residual metallic potassium may intercalate between the carbon layers, resulting in the expansion of the

bio-char structure [59].

FESEM micrographs of the powders before the milling process, reported in Fig. 1, provide a visual insight into the morphology of lignin-derived HCs (L-HCs). The effects of KOH activation and subsequent pyrolysis are evident, as the structure is marked by gas bubbling patterns characteristic of the gaseous species evolution of this activation process. To reduce particle size and enhance electrode homogeneity, a milling process was performed to fragment the framework into smaller particles, as shown in the micrographs in Fig. S1.

The EDS maps of SW11, HW11, SW21, and HW21 powder materials, reported in Figs. S2, S3, S4, and S5, respectively, reveal a generally uniform distribution of carbon, oxygen, and potassium across the particle surfaces for all samples, indicating that the activation process does not induce significant elemental segregation. However, localized spots exhibiting a higher concentration of silicon were detected in both SW and HW carbons. These Si-rich regions correspond to areas where the oxygen signal is also slightly enhanced, suggesting that these features may originate from residual silica, derived from the biomass precursor. Fig. 2a displays the N_2 adsorption/desorption isotherms of the studied materials. According to the International Union of Pure and Applied Chemistry standards, they can be classified as Type-I [60]. This type of isotherm shows a significant nitrogen adsorption at low relative pressure values and becomes nearly horizontal, suggesting that the L-HCs exhibit an elevated amount of micropores [61]. In addition, in the samples that were activated with the 2:1 ratio, the isotherms present a H4 hysteresis loop at a p/p^0 range of 0.4–1.0, implying the presence of mesopores with mixed slit/cylindrical-like geometry. The BET method confirmed that 2:1 L-HCs exhibited a higher surface area with respect to the 1:1 materials due to the action of a higher amount of KOH [56]. Specifically, the calculation of the BET surface area gave the following values: $601 \text{ m}^2 \text{ g}^{-1}$, $664 \text{ m}^2 \text{ g}^{-1}$, $1127 \text{ m}^2 \text{ g}^{-1}$, and $1304 \text{ m}^2 \text{ g}^{-1}$ for SW11, HW11, SW21, and HW21 samples, respectively. These results are reported together with microporous and mesoporous surface and total, microporous, and mesoporous volume values, in Table S1. The isotherm analysis shows that HW-derived materials have a larger surface area than SW-derived ones, for each KOH/biomass ratio used. The PSD shown in Fig. S6 confirms that all the samples predominantly contain pores with diameters smaller than 1 nm. The nanoporous architecture of the L-HCs

evidences a high surface area, providing numerous available reaction sites for potassium ions [62]. They also function as ion-buffering reservoirs, which help accommodating volume changes during cycling, thereby maintaining structural integrity and improving specific capacity [29]. Diffractograms of the four powders in Fig. 2b exhibit two main peaks centered at around 25° and 44° , which are typical of HCs (standard reference PDF #75-1621) and correspond to the (002) and (101) planes of the graphitic structure, respectively [63–66]. The broad shape of these peaks confirms the amorphous structure of the studied materials and suggests a higher degrees of graphitization for HW materials, having slightly narrower peaks with respect to SWs. Additionally, the (002) peak shifts suggest different interlayer distances for all the L-HCs [64]. Applying Bragg's law to each peak, the interlayer distances for the different samples result equal to 0.36 nm, 0.35 nm, 0.40 nm, and 0.41 nm for HW21, SW21, HW11, and SW11 samples, respectively. It can be observed that the materials with a KOH to biomass 1:1 ratio presented a wider interlayer distance than those activated using a 2:1 proportion; this difference will be further discussed within the XPS result analysis. It should be remarked that all the L-HCs samples exhibited a larger interlayer distance than highly ordered graphite (*i.e.*, 0.33 nm) [67]. This feature is beneficial for K-ion intercalation since this structure is suitable for bigger ions, avoiding structural collapse and consequently enhancing cycling stability [14].

Raman spectra of the milled powder materials (Fig. S7) exhibit two characteristic peaks, D and G, located at approximately 1350 cm^{-1} and 1590 cm^{-1} , respectively, which are typical of carbonaceous structures. The G band corresponds to sp^2 -type bonds, while the D band is associated with structural defects and edges, which are rich in O-containing functional groups within the carbon matrix. The ratio between the intensity of these two peaks (I_D/I_G) was calculated to assess the disorder degree and the proportion of sp^3/sp^2 bonds. As it can be seen, all samples exhibited similar I_D/I_G ratios, with a prominent D band contribution, confirming the amorphous and defects-abundant nature of all of them.

To better understand the composition of the biocarbons and their graphitization degree, XPS spectra of L-HCs powders were acquired. The XPS survey spectra and relative atomic concentrations, reported in Fig. S8 and Table S2, respectively, shed light on the surface chemical composition of the studied materials. The main elements present in the

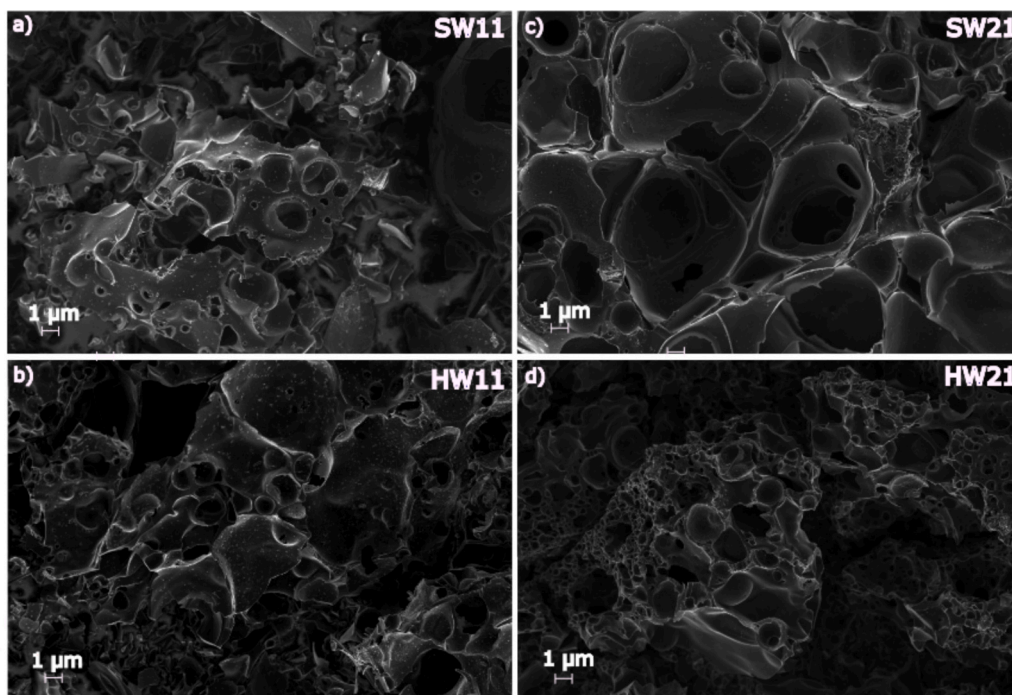


Fig. 1. FESEM micrographs with magnification of 10k of powders before the ball milling treatment: a) SW11, b) HW11, c) SW21, d) HW21.

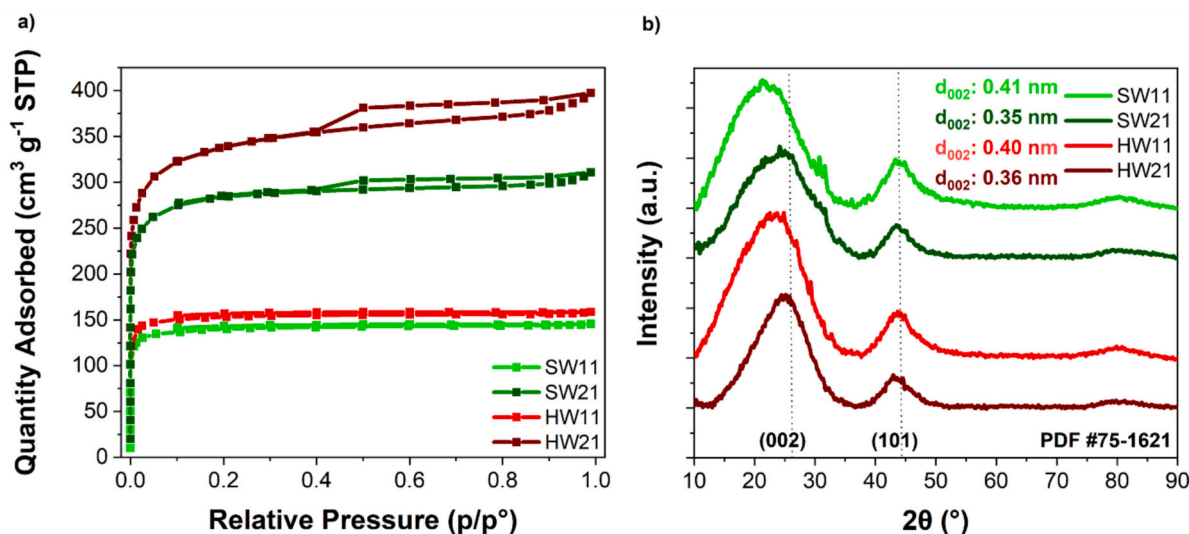


Fig. 2. a) N₂ adsorption/desorption isothermal curves; b) XRD patterns of SW11 (light green lines), HW11 (red lines), SW21 (dark green lines), and HW21 (brown lines).

samples are carbon and oxygen, although the analysis also evidenced the presence of a small amount of potassium. It can be observed that the 2:1 L-HCs displayed higher concentrations of potassium. This could be attributed to residual potassium-based products, suggesting that the effects of a higher KOH to biomass ratio influence the chemical composition of the samples. In addition, the presence of trace silicon species was detected, consistently with EDS mapping results.

HR spectra were performed in the C 1s and K 2p regions, to study the functional groups present in the samples, related to these two elements. The spectra and the relative data extracted from the deconvolution of

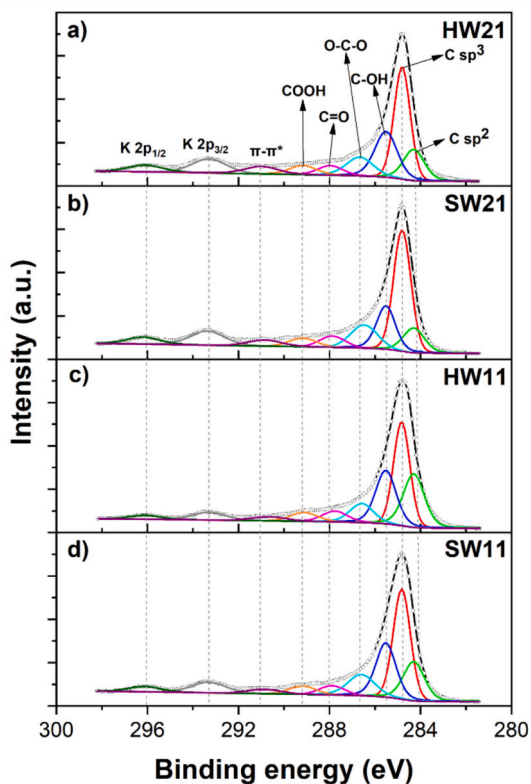


Fig. 3. C 1s and K 2p HR XPS spectra for a) HW21, b) SW21, c) HW11, and d) SW11 powders.

the curves, reported in Fig. 3 and Table S3, respectively, show the presence of a main peak at 284.8 eV attributed to C sp³ aliphatic carbon, for all the samples. This is representative of the amorphous structures, while the peak at 284.4 eV, attributed to the C sp² carbon, is representative of the highly ordered graphitic structures [68]. The evaluation of the ratio between the intensity of these two peaks has been useful to estimate the graphitization degree of the L-HCs. The values of the C sp³/C sp² ratio correspond to 2.08, 1.37, 3.69, and 2.54 for SW11, HW11, SW21, and HW21, respectively. These data evidence that, at the same KOH ratio, HW materials exhibited a higher graphitization degree than SW ones, validating the XRD analysis shown in Fig. 2b. Furthermore, each composition at 1:1 ratio shows a C sp³/C sp² value lower than those with 2:1 ratio, which could imply that the 1:1 samples are more conductive. The other functional groups detected by the analysis are mostly O-groups (–COOH, O–C–O, C=O, C–OH) [57,68]. As previously discussed in the activation mechanism section, KOH activation can modify the amount of oxygen-containing functional groups [72]. This effect is evidenced in Table S3, which shows that samples subjected to milder activation contain a higher total oxygen content. This greater amount of oxygen species likely accounts for the larger interlayer distances observed in the XRD (Fig. 2b) for 1:1 samples, as these functional groups physically expand the carbon layers [69]. Additionally, these functional groups provide a greater number of active sites for K⁺ adsorption and consequently could contribute to an additional capacity. It can be observed that there is a higher concentration of O–C–O bonds compared to C=O, so the XPS analysis corroborates the proposed mechanism for biomass activation [56]. In this mechanism, KOH treatment induces the cleavage of C=O double bonds and promotes, at their expense, the increased formation of O–C–O bonds. A large peak related to the C–OH bonds is also present, along with two small peaks related to potassium-based compounds derived from the activation with KOH [70]. These two latter peaks from residual potassium compounds are more pronounced for the 2:1 ratio, corroborating the data in Table S2.

HCs energy storage mechanism strongly depends on the composition and microstructure of the materials. For instance, the graphitization degree significantly impacts the dominant storage process: in highly graphitized HCs, intercalation is the primary mechanism, whereas in less graphitized structures pseudocapacitive storage becomes more prominent. Furthermore, a high graphitization degree can accelerate the electron conduction rate, but it does not promote the K-ion diffusion rate due to the long graphitic interlayer lengths [20]. It is still not clear which are the best structural parameters that allow the battery cells to perform

better, because usually these materials are very different among them and present different storage behaviors, with many factors simultaneously playing a crucial role. Comprehensive electrochemical characterization may offer some critical insight into achieving the optimal compromise between these factors for HCs used as anodic materials for KIBs [16,71].

3.2. Electrochemical characterization

This section presents the evaluation of biocarbon-based electrodes, with subsequent detailed characterization of the best performing samples. The aim is to investigate the K-ion storage mechanisms and

determine the factors that mostly affect the electrochemical behavior of the cells; this was initially assessed through galvanostatic discharge/charge tests. The cycling performances reported in Fig. 4a highlight remarkable cycling stability for all the electrodes and the superior performances of the materials that were activated using a 1:1 ratio, which exhibited the highest specific capacities. SW11 gave the best electrochemical performance, delivering a reversible capacity of 118.5 mAh g⁻¹ after 10 cycles and retaining 94.2% of this value after 100 cycles. The higher capacities and the elevated cycling stability of the 1:1 L-HCs could be correlated to the larger interplanar distance of the pseudo-graphitic arrangement, computed from the diffractograms in Fig. 2b. Particularly, after 100 cycles SW11 and HW11 presented specific

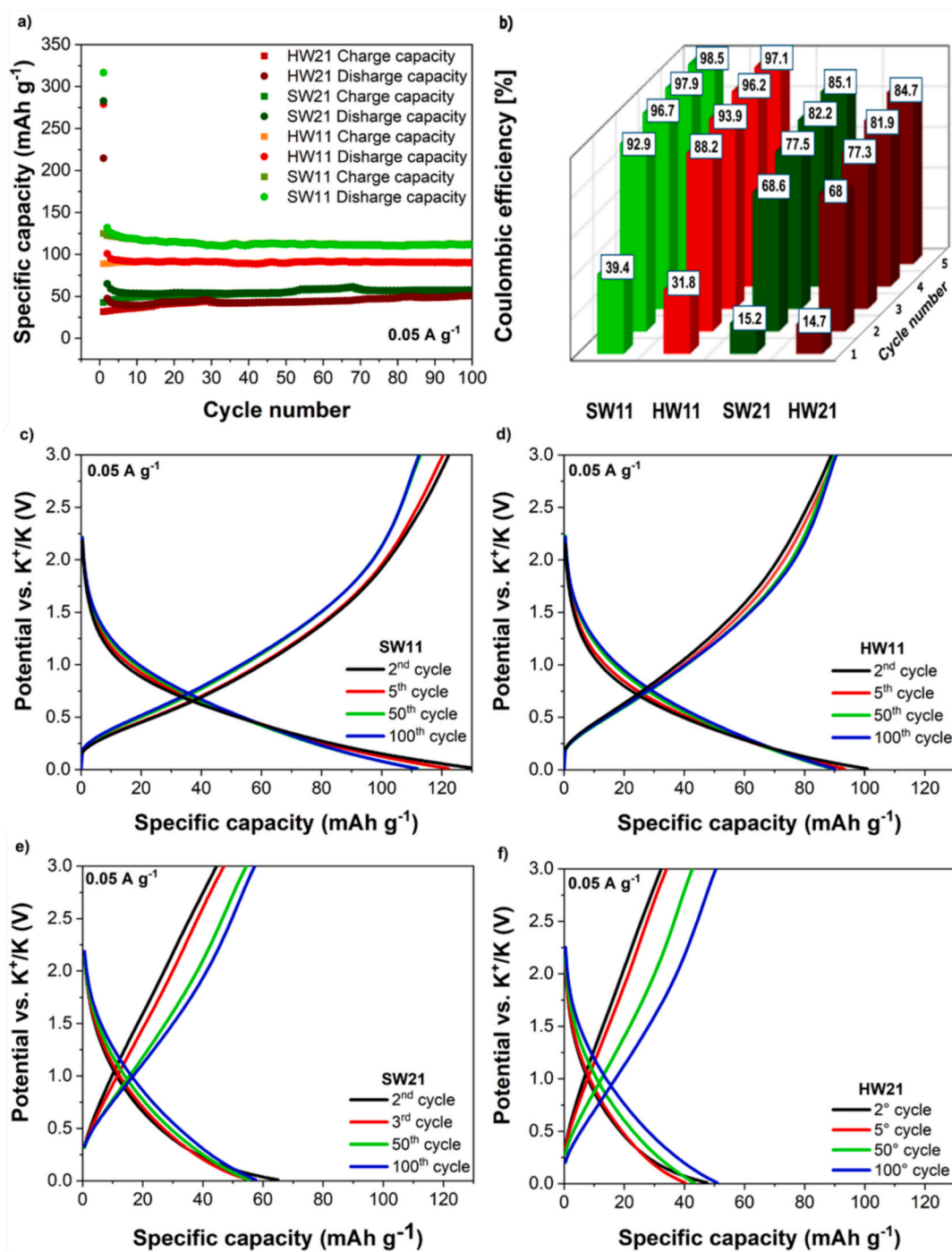


Fig. 4. a) Cycling performances and b) initial CE values for half-cells assembled with the four different biomass-derived materials. Galvanostatic profiles for c) SW11, d) HW11, e) SW21, and f) HW21.

capacity values equal to 111.8 mAh g⁻¹ and 90.9 mAh g⁻¹, respectively. In contrast, the 2:1 L-HC samples showed nearly half of 1:1 values, specifically 53.6 mAh g⁻¹ for SW21 and 39.4 mAh g⁻¹ for HW21.

In full-cell configurations, where potassium-ion availability is limited compared to half-cell systems, Coulombic efficiency (CE) becomes a critical parameter for evaluating battery performance. As shown in Fig. 4b, the CE of all L-HCs-based electrodes is significantly low in the first cycle, particularly for the 2:1 materials. Nonetheless, it can be observed that the CE rapidly increases and stabilizes at higher values of 98% and 97% for SW11 and HW11, respectively, after 5 cycles. The 2:1 L-HCs, on the other hand, demonstrated a slower increase of CE from the first cycle, also taking into account that the initial CE was even lower in these cases. The overall trends of CE during cycling are shown in Fig. S9, which also highlights the differing rates of efficiency increase between the 2:1 and 1:1 L-HC samples. Low CEs can significantly reduce the effective use of active material and, consequently, the energy density of the cell [72]. Usually, HCs deliver low initial CE due to irreversible electrolyte decomposition occurring on the high surface area electrodes [16,73]. The reduction of electrolyte components is thermodynamically unavoidable; however, it prevents further electrolyte decomposition, promoting the cyclic stability of the cell [74]. Since the LUMO levels of electrolyte components are below the Fermi level of the anode, this drives their initial decomposition and the subsequent passivating SEI formation, as further discussed in Section 3.4. The materials exhibit a relatively high specific surface area, which provides extended active sites for K-ion storage, but also for the electrolyte decomposition reactions. As a result, high irreversible capacity related to the SEI layer formation is lost during the first cycles, leading to low ICE [75]. The SW11 and HW11 electrodes, which exhibit a moderate surface area (*i.e.*, 601 m² g⁻¹ and 664 m² g⁻¹, respectively), show higher ICE value (*i.e.*, 39.4% and 31.8%, respectively) and lower irreversible capacity losses, indicating an improved combination of structural and electrochemical properties. In contrast, the higher surface area of the 2:1 L-HCs promotes greater electrolyte decomposition during SEI layer formation. This is supported by the data presented in Table 1, as well as by the large plateaus observed in the first discharge profiles reported in Fig. S10.

Turbodisordered carbons with high surface area are a promising option for addressing K-ion storage challenges; however, their typically low initial CE has prompted several mitigation strategies, ranging from the use of *in-situ* sacrificial additives [76] to the formation of *ex-situ* artificial SEI layers [77,78]. However, the discussion of these strategies falls outside the scope of this study.

The charge/discharge profiles shown in Fig. 4c–f are characterized by near-sloped curves that are indicative of a pseudocapacitive behavior [79] and pronounced electrochemical reversibility upon cycling. The close overlap between the charge and discharge curves (especially for HW11 and SW11) suggests minimal contribution from irreversible capacity losses beyond the second cycle. This behavior, along with the significant irreversible capacity loss during the first discharge, reported in Fig. S10, implies that most of the SEI layer formation occurs during this initial cycle.

Among the samples, SW11 exhibited the best electrochemical performance, followed by HW11, owing to its distinctive structural characteristics. As shown in Fig. 2, SW11 possesses the lowest surface area (601 m² g⁻¹) and the largest interplanar spacing (0.41 nm), while HW11 displays similar values (664 m² g⁻¹ and 0.40 nm, respectively). The expanded interlayer distance facilitated efficient potassium-ion

Table 1

Specific capacity values in the first and second discharge and relative irreversible losses for the four investigated materials.

	SW11	HW11	SW21	HW21
Discharge capacity at 1st cycle [mAh g ⁻¹]	316.5	278.9	282.7	214.7
Discharge capacity at 2nd cycle [mAh g ⁻¹]	131.7	100.9	64.9	47.5
Capacity loss [%]	58	64	77	78

intercalation and diffusion within the carbon matrix, thereby enhancing ion transport kinetics and cycling stability. Meanwhile, the moderate surface area helps to minimize electrolyte decomposition during the SEI layer formation, contributing to the rapid increase in CE during the initial cycles. Once it was established that the L-HCs with a KOH:biomass ratio of 1:1 outperformed the other materials, and the possible reasons for this behavior were identified, the study proceeded to the electrochemical characterization of the best-performing samples (*i.e.*, HW11 and SW11) to further investigate their charge storage mechanisms and deepen the understanding of their electrochemical behavior.

The long cycling test of HW11 and SW11, reported in Fig. 5a, confirmed the outstanding cycling stability of the selected biocarbons. Indeed, SW11 and HW11 exhibited specific capacities of 105.2 mAh g⁻¹ and 85.3 mAh g⁻¹ after 500 cycles, retaining 88.8% and 93.3% of their capacity at the 10th cycle, respectively. Charge transfer resistance is another critical parameter, as it is essential for the conduction of the charges during charge and discharge cycles. Therefore, it plays a critical role in determining the overall electrochemical performance [80]. EIS measurements were employed to evaluate the internal resistance to the charge transfer through the interfaces. The data obtained from EIS measurements on SW11- and HW11-based systems were collected after the 20th cycle, when the SEI layer and the interfaces are formed and stable. The Nyquist plots of SW and HW electrodes, together with the fitted curves and equivalent circuit model, are shown in Fig. 5b. Both impedance spectra display two partially overlapping, depressed semicircles in the high to middle frequency region and a sloped line at low frequencies. The initial intercept of the curve corresponds to the bulk resistance (R1), primarily associated with ion conduction through the electrolyte. The semicircles in the mid-frequency region provide information on the charge-transfer resistance at the electrode/electrolyte interface and the ion diffusion within the electrode material. Accordingly, the equivalent circuit includes a parallel combination of a charge-transfer resistance and a constant phase element (R2||Q2), representing the SEI layer response. The second process is modeled by a more complex element, in which a charge-transfer resistance and a Warburg diffusion element [(R3–W3)] are placed in parallel with a constant phase element (Q3), describing the Faradaic reaction and ion diffusion through the porous carbon framework. The fitted parameters, along with their associated uncertainties, are shown in Table S4 for SW11 and in Table S5 for HW11. The good agreement between experimental and simulated spectra confirms the validity of the selected model. Comparing the plot of SW11 and HW11 in Fig. 5b and the values in Tables S4 and S5, it is clear that the diameter of the first semicircle of HW11 is larger than that of SW11. This indicates that HW11 has a higher total resistance to charge transfer, likely due to differences in SEI layer thickness, composition, and morphology. Instead, as it was already mentioned, the low frequency part of the graph is associated with the Warburg impedance and reflects the diffusion of K ions within the electrode [81]. The diffusion coefficient (D) of the ions can be calculated by using Eq. (1) [82]:

$$D = (0.5 \cdot R^2 \cdot T^2) / (A^2 \cdot n^4 \cdot (Fa)^4 \cdot (Ck)^2 \cdot \sigma^2) \quad (1)$$

where σ is the Warburg's coefficient obtained by the equivalent circuit fitting (W3), R represents the gas constant (*i.e.*, 8.314 J mol⁻¹ K⁻¹), T the absolute temperature (*i.e.*, 298 K), A the surface area of the electrode (*i.e.*, 1.77 cm²), n is the electronic transfer number, which is usually equal to 1 for simplicity, Fa the Faraday's constant (*i.e.*, 96500 C mol⁻¹), and Ck the concentration of K⁺ ions in the electrolyte (*i.e.*, 1 × 10⁻³ mol cm⁻³). Analysis of the measured data using these calculations demonstrated that SW11 possessed a higher D within the electrode material than HW11. Specifically, the D values are 1.10 × 10⁻¹² cm² s⁻¹ and 1.92 × 10⁻¹³ cm² s⁻¹ for SW11 and HW11, respectively. As it can be noticed by the aforementioned results, SW11 exhibited a D value that was one order of magnitude higher than that of HW11 [83]. The rate performance data presented in Fig. 5c corroborate these observations,

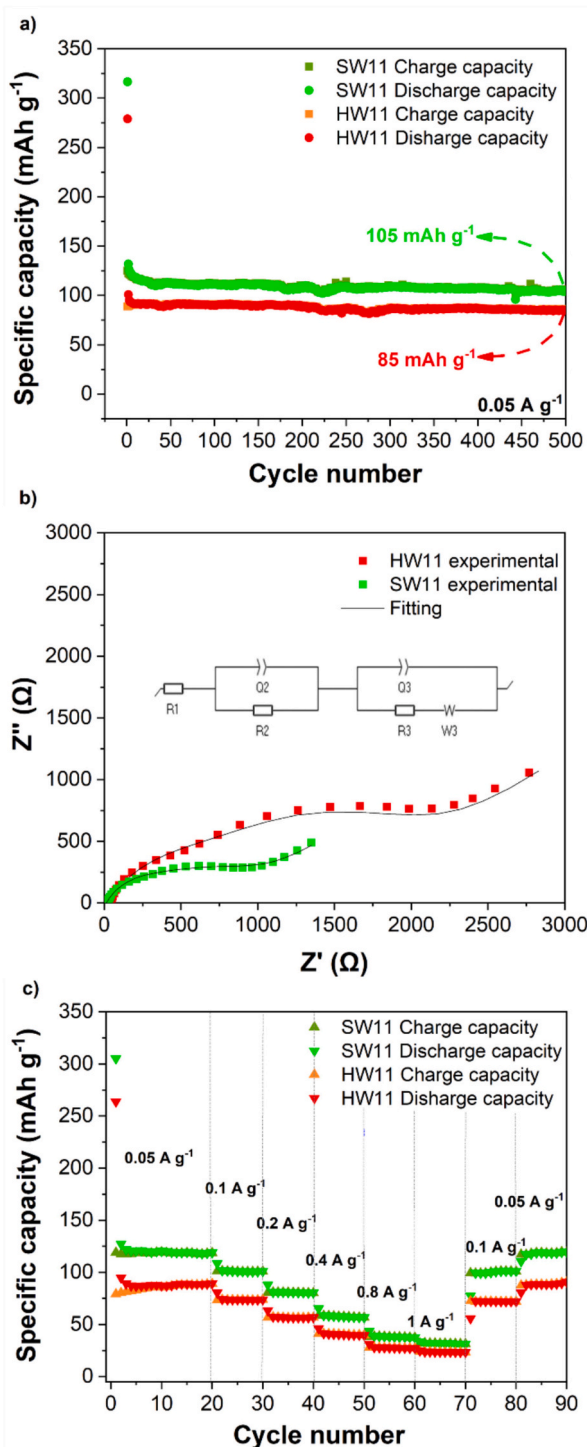


Fig. 5. In-depth electrochemical characterization for SW11 and HW11: a) long cycling performances; b) Experimental (symbols) and fitted (solid lines) Nyquist plots of EIS measured after 20 cycles. Inset: equivalent circuit model used for fitting ($R1-(R2||Q2)-(R3-W3)||Q3$); c) rate performances.

demonstrating that SW11 lower $R1$, $R2$, and $R3$ as well as higher D coefficient translate into superior electrochemical kinetics. Indeed, SW11 maintained the superior response also at higher current rates where faster ion transport is essential, to assure good capacities even under more demanding conditions. Furthermore, both materials demonstrated excellent cycling stability; despite the different current densities, both L-HCs effectively recovered their initial specific capacity values. To better quantify the rate capability, Table S6 reports the

specific discharge capacities of SW11 and HW11 electrodes at various current densities and capacity recovery values after the current density was returned to the initial rate, expressed as a percentage of the baseline capacity at 0.05 A g^{-1} . The resilience after the current change underscores the potential of L-HCs for applications requiring reliable performance under variable operating conditions.

3.3. Storage mechanism analysis

CV is a very useful technique to analyze the electrochemical behavior of redox materials during discharge and charge cycles, and it also provides insights into SEI layer formation dynamics. In particular, the voltammograms of the first 5 cycles reported in Fig. 6a,b support the hypothesis of the fast formation of a stable SEI layer for both L-HCs, reaching reversibility as early as the 2nd cycle. At 1 V, a subtle peak in the reduction branch of the first cycle can be observed, precisely at the same voltage value where a variation in the slope for discharge profiles of the first cycle was registered, as reported in Fig. S10. After the irreversible reactions relative to the reduction branch of the first cycle, the following voltammograms showed a smaller area, and the curves almost overlapped. This indicated that the SEI layer mainly formed during the first reduction, which is consistent with the low ICE reported in Section 3.2. Regarding the oxidation branch of both samples, a broad and small peak was observed between 0.01 and 0.60 V. This peak is representative of the deintercalation processes occurring in this voltage window, and its broadness expressed the graduality of the de-intercalation of K-ions from the pseudo-graphitic structure [84]. As it can be observed, this peak is slightly more pronounced for SW11 than HW11, suggesting that SW11 undergoes faster deintercalation of K-ions. This observation is consistent with the results in Fig. 2b, which show the slightly larger interlayer spacing of SW11 compared to HW11. As it can be seen, this factor is crucial to facilitate the accommodation of the ions during intercalation and deintercalation. Moreover, the voltammograms do not display any other sharp peak apart from the first reduction. So, the CV shape, together with the galvanostatic profiles of Fig. 4c-f, strongly suggests a pseudocapacitive behavior for the investigated materials. To better understand this behavior, it is essential to examine the charge storage mechanisms governing the electrochemical response of these materials.

Charge storage mechanisms can be broadly categorized into two types: Faradaic (battery-like) and capacitor-like materials. Faradaic materials store charge *via* electron transfer reactions, characterized by galvanostatic charge/discharge profiles with distinct plateaus and voltammograms displaying sharp, well-separated redox peaks. Conversely, capacitor-like materials store charge through surface-controlled processes, where ions accumulate at the electric double-layer interface, resulting in a linear voltage/time response and rectangular-shaped CV curves. Materials exhibiting intermediate behavior between these two mechanisms are classified as pseudocapacitive. The term was introduced by Conway in 1980 [85] and nowadays is widely used to describe materials with intermediate behaviors. Thereby, the charge storage for pseudocapacitive materials is entirely Faradic, but the difference with battery-like materials is that the redox reactions occur mainly on the surface instead of the inner regions of the material, making their electrochemical response similar to that of the capacitor-like [79]. The analysis of the current response during CVs at increasing scan rates is helpful to clarify the behavior of these materials. Faradaic storage is intrinsically slower than surface-driven storage mechanism, because the ions need to diffuse inside the electrode materials to trigger the redox reactions. Consequently, Faradaic processes are more evident at lower scan rates while surface-driven storage prevails at higher scan rates. Cottrell's equation [79] states that the capacitive current contribution is linearly proportional to the scan rate, while the diffusional one is proportional to the square root of the scan rate. Therefore, the total current response can be split into two terms, the capacitive and diffusional currents, as reported in Eq. (2):

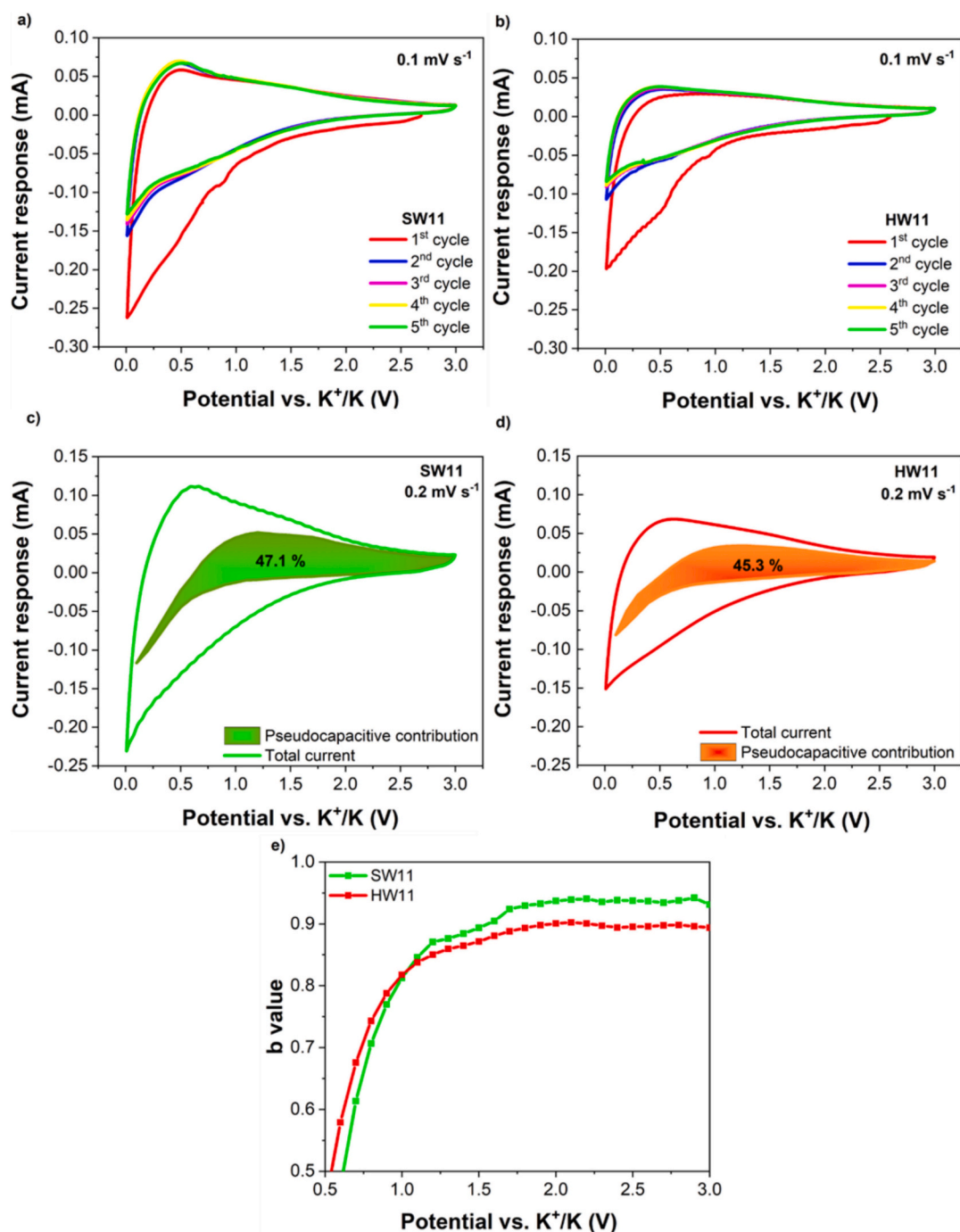


Fig. 6. CV curves at the constant scan rate of 0.1 mV s^{-1} for 5 cycles for a) SW11 and b) HW11. Dunn's method applied to VSCV for c) SW11 and d) HW11; the filled areas show the pseudocapacitive contribution to the total charge storage. e) Oxidation branch b values plot.

$$i = i_{\text{capacitive}} + i_{\text{diffusional}} \quad (2)$$

To this purpose, VSCVs were collected to quantitatively evaluate the pseudocapacitive contribution of the investigated materials, applying Dunn's methods [86]. The results obtained from this analysis are shown in Fig. 6c–d, while the corresponding VSCV measurements are presented in Fig. S11. A trend of increasing response current module with rising scan rate is observed in the VSCV, and this behavior is present in both the positive and negative branch of the curves. The CVs across the varied scan rates present similar shapes, evidencing the absence of reaction selectivity. Furthermore, a current peak shift can be noticed in both materials, which is induced by a diffusional storage mechanism [84]. Dunn's method graphs in Fig. 6c–d report the pseudocapacitive

contribution in the shaded areas. This method not only enables the quantification of the pseudocapacitive contribution, but also allows to identify the voltage intervals where the behavior is driven by diffusion or pseudocapacitive processes. In this case, the pseudocapacitive contribution is predominant in the higher-voltages, while diffusion-controlled mechanisms prevail at lower voltages, as expected since intercalation/deintercalation processes occur in these potential regions. Dunn's analysis evidenced an important pseudocapacitive contribution to the total charge storage, specifically 47.1% for SW11 and 45.3% for HW11.

To further validate the results obtained by Dunn's method, the calculation of the b value has been performed. This value can be

obtained with a rearrangement of Eq. (3), using the empirical formula reported in Eq. (3):

$$i = a \cdot \nu^b \quad (3)$$

where ν is the scan rate, a and b are adjustable values. Taking the logarithm of both sides of Eq. (3) renders Eq. (4).

$$\log(i) = \log(a) + b \cdot \log(\nu) \quad (4)$$

Analyzing b values can offer deeper insights into the contributions of capacitive and diffusion-controlled processes across different voltage regions of the voltammograms. Hence, b value equal to 1 indicates a linear relationship between current and scan rate, typical of a capacitive storage mechanism. In contrast, a b value equal to 0.5 suggests a current proportional to the square root of the scan rate, indicative of diffusion-controlled behavior, while b values between 0.5 and 1 are representative of a mixed charge storage mechanism. The graph reported in Fig. 6e shows the trend of the b values along the oxidation branch for SW11 and HW11, which are quite similar. SW11 presented a slightly higher pseudocapacitive contribution compared to HW11 and in both L-HCs this contribution was prominently located in the high-voltage region. Conversely, the diffusional contribution started to be more predominant at potentials lower than 1 V. These results are in line with Dunn's method. Therefore, the quantitative analysis of the charge storage mechanism suggests that the materials utilize a combination of both pseudocapacitive and Faradaic charge storage mechanisms, providing satisfactory specific capacity and outstanding stability [87].

To further elucidate the potassium storage mechanism of the best-performing material (*i.e.*, SW11), GITT measurements were conducted. These characterizations were done in cells that had already undergone five galvanostatic cycles at 0.05 A g^{-1} , ensuring the formation of a stable SEI layer. The GITT profiles, reported in Fig. S12, exhibits a near-sloped shape without distinct plateaus, indicative of dominant pseudocapacitive behavior. From the GITT data, the diffusion coefficient of K-ions within the porous carbon matrix was calculated, following the procedure reported in the literature for porous materials [88]. A schematic explanation of the parameters employed is provided in Fig. S13 and Note 1. The diffusion coefficients were extracted at different potentials (*i.e.*, state of dis/charge) of the discharge and charge, and are shown in Fig. 7a and b, respectively. These plots reveal that diffusion coefficients are higher at elevated potentials during both charge and discharge. This trend is fully consistent with the Dunn's method analysis, which revealed a predominance of pseudocapacitive storage at higher potentials, where ions mainly adsorb on or desorb from readily accessible surface sites, resulting in higher diffusion coefficients. As the potential decreases, the system progressively shifts toward a diffusion-controlled regime,

reflected in the lower diffusion coefficients associated with ion transport to and from less accessible regions. Specifically, below approximately 1 V during discharge, a significant decrease in the diffusion coefficient is observed, whereas - during charge - the decrease is more gradual and linear.

Additionally, it is noteworthy that the decrease in diffusion coefficient at low potentials is less pronounced than reported in other studies [32,84,89]. This suggests that, even after surface saturation with potassium ions (*i.e.*, potential < 0.4 V), diffusion remains relatively efficient. It is important to point out that the diffusion coefficients calculated from EIS measurements are significantly lower than those obtained from the GITT. This discrepancy arises from the fundamentally different nature of the two techniques. GITT probes ion diffusion under quasi-equilibrium conditions, capturing the diffusion of potassium ions within the electrode material. In contrast, EIS measures the system response for the highest voltage values (*i.e.*, equilibrium potential at the end of charge) and over a broad frequency range, encompassing multiple processes such as charge-transfer resistance, SEI layer resistance, and ion diffusion through complex porous structures. The diffusion coefficients derived from EIS are therefore influenced by these additional resistive and interfacial effects, resulting in lower diffusion values. Consequently, the combined use of GITT and EIS provides a more comprehensive understanding of ion transport dynamics, highlighting both diffusion and interfacial limitations in lignin-derived HC electrodes.

3.4. Physicochemical electrodes characterization

The SEI layer is crucial to the cell functioning, as it allows the transport of ions while also acting as an electronic insulator between the electrode and the electrolyte. Its spontaneous formation causes an irreversible capacity loss, but prevents further electrolyte decomposition, promoting the cycling stability of the cell. It is widely demonstrated that the SEI layer characteristics are paramount for the electrochemical performance of the cell [74]; in fact, the SEI layer, which is usually formed on materials with a large surface area, is even more determinant for the electrochemical response of the electrode. For this reason, a characterization of the passivation layer is needed to understand its formation mechanism and composition. The SEI layer is constituted by the products of the reduction of the electrolyte: when the anode Fermi level is higher than the lowest unoccupied molecular orbital (LUMO) of the electrolyte, an electron can be spontaneously transferred from the electrode material to the electrolyte compounds [90]. In this case, the salt is the component with the lowest LUMO (0.51 eV), followed by the solvents EC (0.84 eV) and DEC (1.01 eV). Considering this information, it could be assumed that the formation of an inner SEI layer occurred,

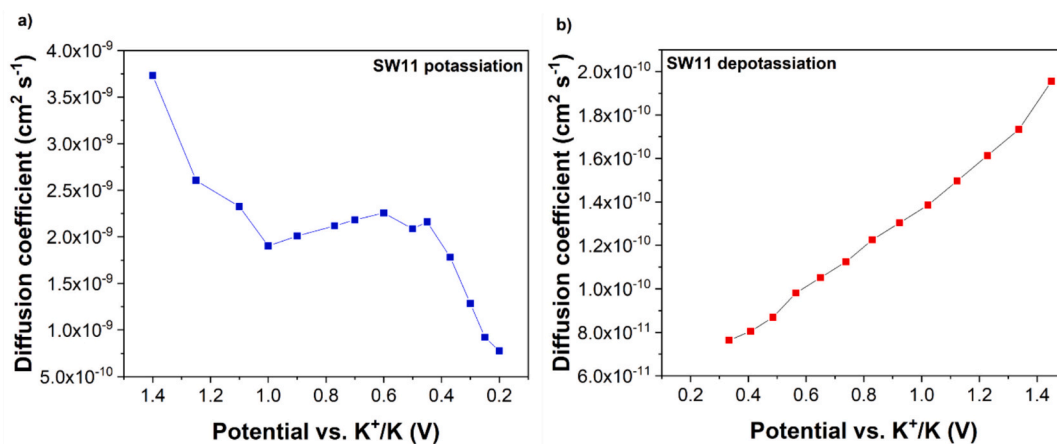


Fig. 7. K-ion diffusion coefficient as a function of potential for the SW11 electrode during a) discharge (potassiation) and b) charge (depotassiation), obtained from GITT data after 5 galvanostatic cycles at 0.05 A g^{-1} .

constituted mainly by inorganic KFSI decomposition products, as well as an outer organic SEI layer is composed by solvent reduction products. Specifically, the decomposition of the solvent was supposed to form different families of components like ROK, RCO_2K , ROCO_2K , and K_2CO_3 , where R is a low molecular weight alkyl group [91]. However, the closeness of the LUMO levels between the different electrolyte components also suggested their almost simultaneous decomposition. This fact implies that the formation of a mosaic structure with a random distribution of organic and inorganic components in the SEI films was more likely to occur [92]. XPS measurements were performed on the pristine and cycled electrodes (after 30 cycles) to elucidate the chemical nature of the SEI layer components and to correlate them with the electrochemical performance of the cells.

The XPS spectra of the C 1s-K 2p region of the pristine electrodes, reported in Fig. 8a for SW11 and Fig. S14a for HW11, reveal distinctive peaks at approximately 290 eV, attributed to the FC-OH and FC_2 functional groups. These signatures are consistent with PVDF, derived from the electrode binder. The HR deconvolution data presented in Table S7 report the relative percentage of these compounds. The relative atomic concentration analysis, extracted from the survey spectra and reported in Table S8, also shows the presence and significance of the F 1s band, which further supports the identification of PVDF. In contrast, in the C 1s - K 2p HR XPS spectra of the cycled electrodes, reported in Fig. 8b for SW11 and Fig. S14b for HW11, the PVDF-related peaks are absent. This finding is further corroborated by the relative atomic concentration analysis of the cycled electrodes, reported in Table S9, which reveals no detectable fluorine compounds in the F 1s spectral region. Concurrently, the data show a marked increase in K-containing species, likely associated with SEI layer components formed during cycling. The

disappearance of the F 1s signatures post-cycling may be attributed to the coverage effect of the SEI layer, which likely masks the PVDF signal [93]. Moreover, the XPS spectra of cycled electrodes combined with HR deconvolution data from Table S10 reveal a predominance of inorganic compounds over organic constituents within the SEI layer. Specifically, KF and K_2CO_3 emerge as the primary components of the SEI layer, aligning with compositional trends reported in prior studies [94–97]. These inorganic compounds are widely reported to contribute positively to the electrochemical stability during cycling [73,98,99], and their passivating behavior positively interacts with the system, promoting the ion conduction. Furthermore, they are stable, thanks to the low solubility in the solvent, so they can form a solid SEI layer that prevents additional electrolyte decomposition and capacity losses. In contrast, organic compounds originating from solvent decomposition promote the formation of an unstable and inefficient part of the SEI layer, but these decomposition pathways also lead to the formation of K_2CO_3 . According to the literature, EC reduction mainly leads to the direct formation of K_2CO_3 and to $\text{CH}_3\text{CH}_2\text{OK}$, while the decomposition of DEC results in the formation of $\text{CH}_3\text{CH}_2\text{OCO}_2\text{K}$, which is further decomposed into K_2CO_3 [91,100].

Furthermore, to corroborate the hypothesis of the formation of a stable SEI layer on the best-performing electrode (SW11), EIS measurements collected after 20 cycles were compared with those obtained after 3 cycles, when the SEI layer is freshly formed. The comparison of the Nyquist plots, reported in Fig. S15, and resistance parameters obtained through equivalent circuit modeling, reported in Table S11, shows no significant increase in internal resistance (respect to the ones shown in Table S4), confirming the stability and persistence of the SEI layer during cycling.

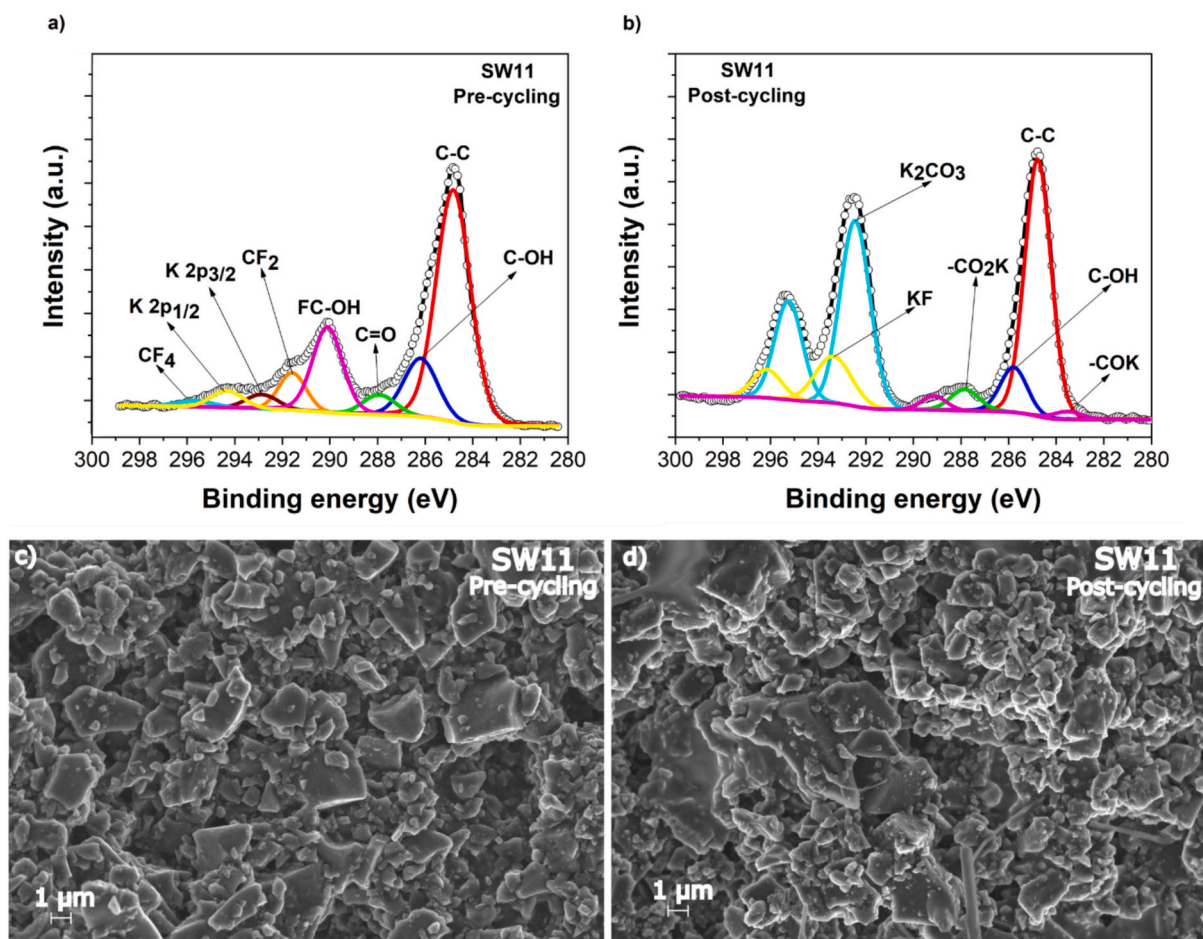


Fig. 8. C 1s - K 2p HR XPS analysis of SW11: a) pre- and b) post-cycled electrodes. FESEM images of HW11: c) pre- and d) post-cycled electrodes (after 30 cycles).

FESEM images of pristine electrodes and after 30 galvanostatic cycles at 0.05 A g^{-1} , respectively, reported for SW11 in Fig. 8c,d and for HW11 in Fig. S16a,b, serve to further support the mechanical stability of the electrodes, which likely contributes to the cycling stability of the cells [101]. A closer examination of the FESEM images reveals that the materials exhibited no cracks, holes, or significant structural changes after the cycling process, which indicates that these electrodes can withstand repeated mechanical stress without structural degradation. Additionally, the materials demonstrated excellent adhesion to the current collector, which is fundamental for efficient electron transfer and overall electrode performance, contributing to the electrode long-term stability.

Raman spectroscopy was conducted on pre- and post-cycled electrodes to evaluate the relative I_D/I_G indexes. The spectra of SW11 and HW11, reported in Fig. S17a,b, show a decrease of the I_D/I_G index for both materials after cycling. This result suggests an increase in the order degree and could be explained by the movement of ions within the disordered structure of the investigated HC, which, during cycling, leads to a rearrangement of the graphene layers in a more ordered structure.

4. Conclusions

This study investigated the feasibility of four different activated L-HCs, derived from biomass, as anode materials for KIBs. The main differences among the studied materials were the fraction of KOH utilized during the synthesis and the type of woody source.

The physicochemical characterization of the powders confirmed that L-HCs with a 2:1 KOH-to-lignin ratio exhibited a higher surface area, but a smaller interplanar distance within the pseudo-graphitic structures, compared to the 1:1 biocarbons.

The investigation evidenced the higher electrochemical performances of the materials with a KOH to biomass ratio equal to 1:1, which exhibit higher specific capacities and enhanced CEs even during the initial cycles. Specifically, SW11 L-HC reported the highest specific capacity value of 118.5 mAh g^{-1} after 10 cycles at 0.05 A g^{-1} , and retained 88.8% of this capacity after a long galvanostatic cycling (500 cycles). However, all the tested materials manifested exceptional and unprecedented cycling stability with respect to the state of the art [102].

The subsequent detailed characterization of the most performing materials allowed shedding light on the charge storage mechanisms and SEI layer formation process. The CV and the galvanostatic profiles furnish significant hints, suggesting the fast formation of a stable SEI layer. CV analysis and GITT confirmed the aforementioned thesis and Dunn's method quantified the pseudocapacitive contribution to the charge storage of SW11 and HW11 being 47.1% and 45.3%, respectively. EIS results confirmed SEI layer stability and indicate a lower resistance to charge transfer and a higher diffusion coefficient for SW11 compared to HW11, which is consistent with the current rate performance. Finally, the XPS analysis on the cycled electrodes demonstrated the presence of stable inorganic components in the SEI layer, like KF and K_2CO_3 , but also of unstable organic components like $\text{CH}_3\text{CH}_2\text{OK}$ and $\text{CH}_3\text{CH}_2\text{OCO}_2\text{K}$, assessing a mosaic structure distribution of the different SEI layer components on the surface. The insights obtained from this study provide valuable guidelines for the rational design of lignin-derived HCs as anode materials for KIBs. The results highlight that both the selection of the lignin precursor and the optimization of the activation ratio are key parameters governing the final carbon structure. Specifically, SW-derived precursors produced more amorphous carbons, which exhibited superior electrochemical behavior with respect to HW electrodes. Meanwhile, milder KOH activation led to moderate BET surface areas for 1:1 samples, offering a well-balanced combination of structural and electrochemical properties. This milder activation also preserved a higher concentration of oxygen-containing functional groups, which supply additional active sites for pseudocapacitive K^+ storage and increase the interplanar distance allowing easier ions intercalation.

Lignin-derived electrodes represent an eco-friendly and cost-

effective alternative to toxic petroleum-based carbons, while demonstrating consistent electrochemical performance. The pseudocapacitive behavior, enabled by the amorphous structure with large interlayer spacing and a nanoporous architecture, together with the rapid formation of a stable SEI layer, allows these electrodes to exhibit outstanding cycling stability even after prolonged testing, as well as capacity values superior to those reported in the literature.

CRedit authorship contribution statement

Antonio Benigno: Writing – original draft, Investigation, Data curation. **Sofia Raviolo:** Writing – original draft, Supervision, Methodology, Investigation, Data curation, Conceptualization. **Sabrina Trano:** Writing – review & editing, Methodology, Investigation. **Sara Domenici:** Writing – review & editing, Investigation. **Micaela Castellino:** Writing – review & editing, Investigation. **Carlotta Francia:** Writing – review & editing, Supervision, Methodology. **Diana Gaspar:** Writing – review & editing, Project administration, Investigation, Conceptualization. **Luís Pereira:** Writing – review & editing, Supervision, Project administration, Funding acquisition, Conceptualization. **Federico Bella:** Writing – review & editing, Supervision, Resources, Project administration, Funding acquisition, Conceptualization.

Declaration of competing interest

The authors declare that they have no known competing financial interests or personal relationships that could have appeared to influence the work reported in this paper.

Acknowledgements

This study was carried out within the «GREEN2MOVE» project [FISA-2022-00983] funded by Ministero dell'Università e della Ricerca (Bando FISA 2022). This work also received funding from the FCT (Fundação para a Ciência e Tecnologia, I.P.) under the projects LA/P/0037/2020, UIDP/50025/2020, and UIDB/50025/2020 of the Associate Laboratory Institute of Nanostructures, Nanomodelling, and Nanofabrication - i3N, project SMART-E (2022.04012.PTDC), and “NGS - New Generation Storage” Innovation Pact (C644936001-00000045), cofounded by the NextGenerationEU, through the investment “Agendas para a Inovação Empresarial” of the Portuguese Recovery and Resilience Plan (PRR). Prof. Julia Amici is kindly thanked for the support in acquiring FESEM micrographs.

Appendix A. Supplementary data

Supplementary data to this article can be found online at <https://doi.org/10.1016/j.cej.2025.172142>.

Data availability

Data will be made available on request.

References

- [1] W.J. Ripple, C. Wolf, J.W. Gregg, J. Rockström, T.M. Newsome, B.E. Law, L. Marques, T.M. Lenton, C. Xu, S. Huq, L. Simons, D. Anthony King, The 2023 state of the climate report: entering uncharted territory, *Bioscience* 73 (2023) 841–850, <https://doi.org/10.1093/BIOSCI/BIAD080>.
- [2] J. Hou, X. Ma, J. Fu, P. Vanaphuti, Z. Yao, Y. Liu, Z. Yang, Y. Wang, A green closed-loop process for selective recycling of lithium from spent lithium-ion batteries, *Green Chem.* 24 (2022) 7049–7060, <https://doi.org/10.1039/d2gc01811j>.
- [3] I. Tsiropoulos, D. Tarvydas, N. Lebedeva, Li-Ion Batteries for Mobility and Stationary Storage Applications Scenarios for Costs and Market Growth, 2018, <https://doi.org/10.2760/87175>.
- [4] H. Vikström, S. Davidsson, M. Höök, Lithium availability and future production outlooks, *Appl. Energy* 110 (2013) 252–266, <https://doi.org/10.1016/j.apenergy.2013.04.005>.

- [5] R.B. Kaunda, Potential environmental impacts of lithium mining, *Journal of Energy and Natural Resources Law* 38 (2020) 237–244, <https://doi.org/10.1080/02646811.2020.1754596>.
- [6] A.K.X. Tan, S. Paul, Beyond lithium: future battery technologies for sustainable energy storage, *Energies* 17 (2024) 5768, <https://doi.org/10.3390/EN17225768>.
- [7] R. Rajagopalan, Y. Tang, X. Ji, C. Jia, H. Wang, Advancements and challenges in potassium ion batteries: a comprehensive review, *Adv. Funct. Mater.* 30 (2020) 1909486, <https://doi.org/10.1002/ADFM.201909486>.
- [8] A. Eftekhari, Potassium secondary cell based on Prussian blue cathode, *J. Power Sources* 126 (2004) 221–228, <https://doi.org/10.1016/J.JPOWSOUR.2003.08.007>.
- [9] X. Min, J. Xiao, M. Fang, W. Wang, Y. Zhao, Y. Liu, A.M. Abdelkader, K. Xi, R. V. Kumar, Z. Huang, Potassium-ion batteries: outlook on present and future technologies, *Energy Environ. Sci.* 14 (2021) 2186–2243, <https://doi.org/10.1039/D0EE02917C>.
- [10] M. Salado, M. Amores, C. Pozo-Gonzalo, M. Forsyth, S. Lanceros-Méndez, Advanced and sustainable functional materials for potassium-ion batteries, *Energy Mater.* 3 (2023) 300037, <https://doi.org/10.20517/ENERGYMATER.2023.36>.
- [11] T. Chuenphan, T. Yurata, T. Sema, B. Chalermisinsuwan, Techno-economic sensitivity analysis for optimization of carbon dioxide capture process by potassium carbonate solution, *Energy* 254 (2022) 124290, <https://doi.org/10.1016/J.JENERGY.2022.124290>.
- [12] Y. Wang, R. Chen, T. Chen, H. Lv, G. Zhu, L. Ma, C. Wang, Z. Jin, J. Liu, Emerging non-lithium ion batteries, *Energy Storage Mater.* 4 (2016) 103–129, <https://doi.org/10.1016/J.JENSM.2016.04.001>.
- [13] Z. Wu, J. Zou, S. Chen, X. Niu, J. Liu, L. Wang, Potassium-ion battery cathodes: past, present, and prospects, *J. Power Sources* 484 (2021) 229307, <https://doi.org/10.1016/J.JPOWSOUR.2020.229307>.
- [14] Y.S. Xu, S.Y. Duan, Y.G. Sun, D.S. Bin, X. Sen Tao, D. Zhang, Y. Liu, A.M. Cao, L. J. Wan, Recent developments in electrode materials for potassium-ion batteries, *J. Mater. Chem. A* 7 (2019) 4334–4352, <https://doi.org/10.1039/C8TA10953B>.
- [15] I. Sultana, M.M. Rahman, Y. Chen, A.M. Glushenkov, Potassium-ion battery anode materials operating through the alloying–dealloying reaction mechanism, *Adv. Funct. Mater.* 28 (2018) 1703857, <https://doi.org/10.1002/ADFM.201703857>.
- [16] J. Yang, Y. Zhai, X. Zhang, E. Zhang, H. Wang, X. Liu, F. Xu, S. Kaskel, Perspective on carbon anode materials for K⁺ storage: balancing the intercalation-controlled and surface-driven behavior, *Adv. Energy Mater.* 11 (2021) 2100856, <https://doi.org/10.1002/AENM.202100856>.
- [17] P. Lian, Y. Dong, Z.S. Wu, S. Zheng, S. Wang, C. Sun, J. Qin, X. Shi, X. Bao, Alkalized Ti₃C₂ MXene nanoribbons with expanded interlayer spacing for high-capacity sodium and potassium ion batteries, *Nano Energy* 40 (2017) 1–8, <https://doi.org/10.1016/J.NANOEN.2017.08.002>.
- [18] H. Gao, T. Zhou, Y. Zheng, Q. Zhang, Y. Liu, J. Chen, H. Liu, Z. Guo, CoS quantum dot nanoclusters for high-energy potassium-ion batteries, *Adv. Funct. Mater.* 27 (2017) 1702634, <https://doi.org/10.1002/ADFM.201702634>.
- [19] Q. Deng, J. Pei, C. Fan, J. Ma, B. Cao, C. Li, Y. Jin, L. Wang, J. Li, Potassium salts of para-aromatic dicarboxylates as the highly efficient organic anodes for low-cost K-ion batteries, *Nano Energy* 33 (2017) 350–355, <https://doi.org/10.1016/J.NANOEN.2017.01.016>.
- [20] L. Zhang, W. Wang, S. Lu, Y. Xiang, Carbon anode materials: a detailed comparison between Na-ion and K-ion batteries, *Adv. Energy Mater.* 11 (2021) 2003640, <https://doi.org/10.1002/AENM.202003640>.
- [21] L. Zhong, W. Zhang, S. Sun, L. Zhao, W. Jian, X. He, Z. Xing, Z. Shi, Y. Chen, H. N. Alshareef, X. Qiu, Engineering of the crystalline lattice of hard carbon anodes toward practical potassium-ion batteries, *Adv. Funct. Mater.* 33 (2023) 2211872, <https://doi.org/10.1002/ADFM.202211872>.
- [22] C. Chen, Z. Wang, B. Zhang, L. Miao, J. Cai, L. Peng, Y. Huang, J. Jiang, Y. Huang, L. Zhang, J. Xie, Nitrogen-rich hard carbon as a highly durable anode for high-power potassium-ion batteries, *Energy Storage Mater.* 8 (2017) 161–168, <https://doi.org/10.1016/J.JENSM.2017.05.010>.
- [23] L. Tan, J. Chen, L. Wang, N. Li, Y. Yang, Y. Chen, L. Guo, X. Ji, Y. Zhu, High-Coulombic-efficiency hard carbon anode material for practical potassium-ion batteries, *Batteries Supercaps* 7 (2024) e202400010, <https://doi.org/10.1002/BATT.202400010>.
- [24] M. Wu, J. Liao, L. Yu, R. Lv, P. Li, W. Sun, R. Tan, X. Duan, L. Zhang, F. Li, J. Kim, K.H. Shin, H. Seok Park, W. Zhang, Z. Guo, H. Wang, Y. Tang, G. Gorgolis, C. Galiotis, J. Ma, Roadmap on carbon materials for energy storage and conversion, *Chem. Asian J.* 15 (2020) 995–1013, <https://doi.org/10.1002/ASIA.201901802>.
- [25] L. Xie, C. Tang, Z. Bi, M. Song, Y. Fan, C. Yan, X. Li, F. Su, Q. Zhang, C. Chen, Hard carbon anodes for next-generation Li-ion batteries: review and perspective, *Adv. Energy Mater.* 11 (2021) 2101650, <https://doi.org/10.1002/AENM.202101650>.
- [26] M. Jiang, N. Sun, T. Li, J. Yu, A. Somoro, M. Jia, B. Xu, Revealing the charge storage mechanism in porous carbon to achieve efficient K ion storage, *Small* 20 (2024) 2401478, <https://doi.org/10.1002/sml.202401478>.
- [27] J. Zhou, S. Guo, Carbon-based anode materials for potassium-ion batteries: from material, mechanism to performance, *SmartMat* 2 (2021) 176–201, <https://doi.org/10.1002/SMM2.1042;ISSUE:ISSUE:DOI>.
- [28] X. Wang, H. Wang, Designing carbon anodes for advanced potassium-ion batteries: materials, modifications, and mechanisms, *Adv. Powder Mater.* 1 (2022) 100057, <https://doi.org/10.1016/J.APMATE.2022.100057>.
- [29] C. Wang, J. Huang, J. Li, L. Cao, Q. Chen, C. Qian, S. Chen, Revealing the effect of nanopores in biomass-derived carbon on its sodium-ion storage behavior, *ChemElectroChem* 7 (2020) 201–211, <https://doi.org/10.1002/CELC.201901829>.
- [30] W. Li, R. Zhang, Z. Chen, B. Fan, K. Xiao, H. Liu, P. Gao, J. Wu, C. Tu, J. Liu, Microstructure-dependent K⁺ storage in porous hard carbon, *Small* 17 (2021) 2100397, <https://doi.org/10.1002/SMLL.202100397>.
- [31] F. Xie, Z. Xu, Z. Guo, M.M. Titirici, Hard carbons for sodium-ion batteries and beyond, *Prog. Energy* 2 (2020) 042002, <https://doi.org/10.1088/2516-1083/ABAF55>.
- [32] S. Tan, H. Yang, Z. Zhang, X. Xu, Y. Xu, J. Zhou, X. Zhou, Z. Pan, X. Rao, Y. Gu, Z. Wang, Y. Wu, X. Liu, Y. Zhang, The progress of hard carbon as an anode material in sodium-ion batteries, *Molecules* 28 (2023) 3134, <https://doi.org/10.3390/MOLECULES28073134>.
- [33] Z. Guo, Z. Xu, F. Xie, J. Jiang, K. Zheng, S. Alabidun, M. Crespo-Ribadeneyra, Y. S. Hu, H. Au, M.M. Titirici, Investigating the superior performance of hard carbon anodes in sodium-ion compared with lithium- and potassium-ion batteries, *Adv. Mater.* 35 (2023) 2304091, <https://doi.org/10.1002/ADMA.202304091>.
- [34] X. Lin, Y. Liu, H. Tan, B. Zhang, Advanced lignin-derived hard carbon for Na-ion batteries and a comparison with Li and K ion storage, *Carbon* 157 (2020) 316–323, <https://doi.org/10.1016/J.CARBON.2019.10.045>.
- [35] T.K. Kumaresan, S.A. Masilamani, K. Raman, S.Z. Karazhanov, R. Subashchandrabose, High performance sodium-ion battery anode using biomass derived hard carbon with engineered defective sites, *Electrochim. Acta* 368 (2021) 137574, <https://doi.org/10.1016/J.ELECTACTA.2020.137574>.
- [36] P.N.Y. Yek, R.K. Liew, M.S. Osman, C.L. Lee, J.H. Chuah, Y.K. Park, S.S. Lam, Microwave steam activation, an innovative pyrolysis approach to convert waste palm shell into highly microporous activated carbon, *J. Environ. Manage.* 236 (2019) 245–253, <https://doi.org/10.1016/J.JENVMAN.2019.01.010>.
- [37] W. Yu, H. Wang, S. Liu, N. Mao, X. Liu, J. Shi, W. Liu, S. Chen, X. Wang, N. O-codoped hierarchical porous carbons derived from algae for high-capacity supercapacitors and battery anodes, *J. Mater. Chem. A* 4 (2016) 5973–5983, <https://doi.org/10.1039/C6TA01821A>.
- [38] T. Liu, X. Li, Biomass-derived nanostructured porous carbons for sodium ion batteries: a review, *Mater. Technol.* 34 (2019) 232–245, <https://doi.org/10.1080/10667857.2018.1545392>.
- [39] H. Lei, J. Li, X. Zhang, L. Ma, Z. Ji, Z. Wang, L. Pan, S. Tan, W. Mai, A review of hard carbon anode: rational design and advanced characterization in potassium ion batteries, *InfoMat* 4 (2022) e12272, <https://doi.org/10.1002/INF2.12272;WGROU:STRING-PUBLICATION>.
- [40] Y. Zhang, D. Qi, Y. Wang, T. Wang, Y. Tian, B. Zhang, N. Wang, *Rhus typhina* wood-based biochar electrodes for high effective potassium storage capacity, *J. Mater. Sci. - Mater. Electron.* 35 (33) (2024) 2136, <https://doi.org/10.1007/S10854-024-13890-W>.
- [41] Z. Wu, J. Zou, Y. Zhang, X. Lin, D. Fry, L. Wang, J. Liu, Lignin-derived hard carbon anode for potassium-ion batteries: interplay among lignin molecular weight, material structures, and storage mechanisms, *Chem. Eng. J.* 427 (2022) 131547, <https://doi.org/10.1016/J.CEJ.2021.131547>.
- [42] Y. Xi, D. Yang, X. Qiu, H. Wang, J. Huang, Q. Li, Renewable lignin-based carbon with a remarkable electrochemical performance from potassium compound activation, *Ind. Crop. Prod.* 124 (2018) 747–754, <https://doi.org/10.1016/J.INDCROP.2018.08.018>.
- [43] A.K. Nanjundam, R.R. Gaddam, A.H. Farokh Naei, P.K. Annamalai, D.P. Dubal, D. J. Martin, Y. Yamauchi, D.J. Searles, X.S. Zhao, Potassium-ion storage in cellulose-derived hard carbon: the role of functional groups, *Batteries Supercaps* 3 (2020) 953–960, <https://doi.org/10.1002/BATT.202000116>.
- [44] J. Chen, L. Tan, C. Lin, Y. Bai, X. Niu, Z. Zhang, N. Li, L. Wang, Y. Wang, X. Ji, Y. Zhu, Graphite-catalyzed carbonization of biowaste unlocks energy-dense, high-rate, and long-lifespan potassium-ion batteries, *Chem. Eng. J.* 515 (2025) 163832, <https://doi.org/10.1016/J.CEJ.2025.163832>.
- [45] M. Härmäs, A. Olgo, A. Adamson, M. Koppel, A. Jänes, Optimizing synthesis temperature for lignin-derived hard carbon anode for high cycling capacity in sodium-ion batteries, *J. Electrochem. Soc.* 171 (2024) 020539, <https://doi.org/10.1149/1945-7111/AD28D7>.
- [46] A. Wang, G. Zhang, M. Li, Y. Sun, Y. Tang, K. Sun, J.M. Lee, G. Fu, J. Jiang, Lignin derived hard carbon for sodium ion batteries: recent advances and future perspectives, *Prog. Mater. Sci.* 152 (2025) 101452, <https://doi.org/10.1016/J.PMATSCI.2025.101452>.
- [47] Ş. Parlayıcı, E. Pehlivan, The importance of sustainable biomass sources in the development of porous carbonaceous materials-synthesis and energy applications: a review, *Univ. J. Catal. Sci.* 1 (2023) 96–109, <https://doi.org/10.37256/ujcs.1220233335>.
- [48] M.-S. Lim, G.H. Lim, Y.-J. Shin, J.-S. Chae, J.-W. Lee, K.C. Roh, Partially graphitic structure-assisted hard carbon derived from lignin for sodium-ion battery anodes, *Energy Mater.* 5 (2025) 500104, <https://doi.org/10.20517/ENERGYMATER.2025.08>.
- [49] M. Staš, M. Auersvald, L. Kejla, D. Vrtiška, J. Kroufek, D. Kubička, Quantitative analysis of pyrolysis bio-oils: a review, *TrAC Trends Anal. Chem.* 126 (2020) 115857, <https://doi.org/10.1016/J.J.TRAC.2020.115857>.
- [50] H. Kawamoto, Lignin pyrolysis reactions, *J. Wood Sci.* 63 (2) (2017) 117–132, <https://doi.org/10.1007/S10086-016-1606-Z>.
- [51] J.E. Murreta, J. Uriarte, D. Compton, R. LaDouceur, J. Kirtley, D. Prieto-Centurion, Effects of lignin syringyl to guaiacyl ratio on cottonwood biochar adsorbent properties and performance, *Sci. Rep.* 14 (1) (2024) 1–13, <https://doi.org/10.1038/s41598-024-70186-z>.
- [52] M.R. Nimlos, R. Martinez, N. Wilson, S.-D. Han, W. Sagues, S. Park, T. Vook, S. C. Dey, M. Regula, Z. Combs, C. Fagerholm, B. Freel, G. Hopkins, T. Vries,

- T. Vries, Carbon anode material from biomass pyrolysis oil, ACS National Meeting (2022).
- [53] H. Lyu, Z. Yu, B. Gao, F. He, J. Huang, J. Tang, B. Shen, Ball-milled biochar for alternative carbon electrode, *Environ. Sci. Pollut. Res.* 26 (2019) 14693–14702, <https://doi.org/10.1007/S11356-019-04899-4/TABLES/2>.
- [54] S. Brunauer, P.H. Emmett, E. Teller, Adsorption of gases in multimolecular layers, *J. Am. Chem. Soc.* 60 (1938) 309–319, <https://doi.org/10.1021/ja01269a023>.
- [55] J.P.L. Gurvitsch, *Chem. Soc. Russ.* 47 (1915) 49.
- [56] W. Chen, M. Gong, K. Li, M. Xia, Z. Chen, H. Xiao, Y. Fang, Y. Chen, H. Yang, H. Chen, Insight into KOH activation mechanism during biomass pyrolysis: chemical reactions between O-containing groups and KOH, *Appl. Energy* 278 (2020) 115730, <https://doi.org/10.1016/J.APENERGY.2020.115730>.
- [57] Z. Li, H. Wu, D. Zhang, Q. Wang, H. Sun, Q. Sun, B. Wang, Revealing the mechanism of oxygen-containing functional groups on the capacitive behavior of activated carbon, *Appl. Surf. Sci.* 657 (2024) 159744, <https://doi.org/10.1016/J.APSUSC.2024.159744>.
- [58] H. Wang, F. Sun, Z. Qu, K. Wang, L. Wang, X. Pi, J. Gao, G. Zhao, Oxygen functional group modification of cellulose-derived hard carbon for enhanced sodium ion storage, *ACS Sustain. Chem. Eng.* 7 (2019) 18554–18565, <https://doi.org/10.1021/ACSUSCHEMENG.9B04676>.
- [59] J. Wang, S. Kaskel, KOH activation of carbon-based materials for energy storage, *J. Mater. Chem.* 22 (2012) 23710–23725, <https://doi.org/10.1039/C2JM34066F>.
- [60] M. Thommes, K. Kaneko, A.V. Neimark, J.P. Olivier, F. Rodriguez-Reinoso, J. Rouquerol, K.S.W. Sing, Physisorption of gases, with special reference to the evaluation of surface area and pore size distribution (IUPAC Technical Report), *Pure Appl. Chem.* 87 (2015) 1051–1069, <https://doi.org/10.1515/PAC-2014-1117/MACHINEREADEABLECTATION/RIS>.
- [61] L.M. Anovitz, D.R. Cole, Characterization and analysis of porosity and pore structures, in: *Pore Scale Geochemical Processes*, *Rev. Mineral. Geochem.* 80, 2015, pp. 61–164, <https://doi.org/10.2138/RMG.2015.80.04>.
- [62] J. Yang, X.Y. Zhou, J. Li, Y.L. Zou, J.J. Tang, Study of nano-porous hard carbons as anode materials for lithium ion batteries, *Mater. Chem. Phys.* 135 (2012) 445–450, <https://doi.org/10.1016/J.MATCHEMPHYS.2012.05.006>.
- [63] J. Kim, S.D. Han, B. Koo, S.H. Lee, J. Yang, Structure dependent electrochemical behaviors of hard carbon anode materials derived from natural polymer for next-generation sodium ion battery, *Polymers* 15 (2023) 4373, <https://doi.org/10.3390/POLYM15224373>.
- [64] P. Bai, Y. He, X. Zou, X. Zhao, P. Xiong, Y. Xu, Elucidation of the sodium-storage mechanism in hard carbons, *Adv. Energy Mater.* 8 (2018) 1703217, <https://doi.org/10.1002/AENM.201703217>.
- [65] Z. Tang, R. Zhang, H. Wang, S. Zhou, Z. Pan, Y. Huang, D. Sun, Y. Tang, X. Ji, K. Amine, M. Shao, Revealing the closed pore formation of waste wood-derived hard carbon for advanced sodium-ion battery, *Nat. Commun.* 14 (1) (2023) 6024, <https://doi.org/10.1038/s41467-023-3967-5>.
- [66] Z. Jian, Z. Xing, C. Bommier, Z. Li, X. Ji, Z. Jian, Z. Xing, C. Bommier, Z. Li, X. Ji, Hard carbon microspheres: potassium-ion anode versus sodium-ion anode, *Adv. Energy Mater.* 6 (2016) 1501874, <https://doi.org/10.1002/AENM.201501874>.
- [67] K. Sasaki, K. Hitachi, Universal layer number in graphite, *Commun. Phys.* 3 (1) (2020) 1–5, <https://doi.org/10.1038/s42005-020-0354-y>.
- [68] S. Raviolo, M.V. Bracamonte, C.A. Calderin, F.P. Cometto, G.L. Luque, A green solution to energy storage: brewers' spent grains biocarbon-silica composites as high-performance lithium-ion batteries anodes, *Energy Technol.* 11 (2023) 2300342, <https://doi.org/10.1002/ENTE.202300342>.
- [69] Y. Bu, K. Li, Z. Xiong, Z. Liang, J. Zhang, Z. Bi, H. Zhang, Evolution of layer distance and structural arrangement of graphene oxide with various oxygen content and functional types in low temperature: a ReaxFF molecular dynamics simulation, *Appl. Surf. Sci.* 572 (2022) 151390, <https://doi.org/10.1016/J.APSUSC.2021.151390>.
- [70] Y. Betancur, A. Sánchez, A. Bueno-López, D. López, Potassium catalytic effect on gasification reactions of coal and coal/biomass blends under oxy-combustion conditions. An isotopic study using ¹³C18O₂, *Energy Fuels* 32 (2018) 2439–2449, <https://doi.org/10.1021/ACS.ENERGYFUELS.7B03399>.
- [71] B. Zhang, C.M. Ghimbeu, C. Laberty, C. Vix-Guterl, J.-M. Tarascon, B. Zhang, M. Tarascon, C.M. Ghimbeu, C. Laberty, C. Vix-Guterl, J.-M. Tarascon, Correlation between microstructure and Na storage behavior in hard carbon, *Adv. Energy Mater.* 6 (2016) 1501588, <https://doi.org/10.1002/AENM.201501588>.
- [72] Y. Wan, Y. Liu, D. Chao, W. Li, D. Zhao, Recent advances in hard carbon anodes with high initial Coulombic efficiency for sodium-ion batteries, *Nano Mater. Sci.* 5 (2023) 189–201, <https://doi.org/10.1016/J.NANOMS.2022.02.001>.
- [73] X. Zhao, Y. Chen, H. Sun, T. Yuan, Y. Gong, X. Liu, T. Chen, Impact of surface structure on SEI for carbon materials in alkali ion batteries: a review, *Batteries* 9 (2023) 226, <https://doi.org/10.3390/batteries9040226>.
- [74] T. Hosaka, K. Kubota, A.S. Hameed, S. Komaba, Research development on K-ion batteries, *Chem. Rev.* 120 (2020) 6358–6466, <https://doi.org/10.1021/acs.chemrev.9b00463>.
- [75] A. Kamiyama, K. Kubota, D. Igarashi, Y. Yoon, Y. Tateyama, H. Ando, K. Gotoh, S. Komaba, MgO-template synthesis of extremely high capacity hard carbon for Na-ion battery, *Angew. Chem. Int. Ed.* 60 (2021) 5114–5120, <https://doi.org/10.1002/ANIE.202013951>.
- [76] S.U. Yoon, H. Kim, H.J. Jin, Y.S. Yun, Effects of fluoroethylene carbonate-induced solid-electrolyte-interface layers on carbon-based anode materials for potassium ion batteries, *Appl. Surf. Sci.* 547 (2021) 149193, <https://doi.org/10.1016/J.APSUSC.2021.149193>.
- [77] H. Wang, J. Hu, J. Dong, K.C. Lau, L. Qin, Y. Lei, B. Li, D. Zhai, Y. Wu, F. Kang, Artificial solid-electrolyte interphase enabled high-capacity and stable cycling potassium metal batteries, *Adv. Energy Mater.* 9 (2019) 1902697, <https://doi.org/10.1002/AENM.201902697>.
- [78] V. Aravindan, Y.S. Lee, S. Madhavi, Best practices for mitigating irreversible capacity loss of negative electrodes in Li-ion batteries, *Adv. Energy Mater.* 7 (2017) 1602607, <https://doi.org/10.1002/AENM.201602607>.
- [79] T.S. Mathis, N. Kurra, X. Wang, D. Pinto, P. Simon, Y. Gogotsi, Energy storage data reporting in perspective—guidelines for interpreting the performance of electrochemical energy storage systems, *Adv. Energy Mater.* 9 (2019) 1902007, <https://doi.org/10.1002/AENM.201902007>.
- [80] Y. Zhang, P. Apostol, D. Rambabu, X. Guo, X. Liu, X. Lin, H. Xie, X. Chen, K. Robeyns, J. Wang, J. Wang, A. Vlad, Ionically conducting Li- and Na-phosphonates as organic electrode materials for rechargeable batteries, *Chem. Sci.* 16 (2025) 1819–1825, <https://doi.org/10.1039/D4SC07732F>.
- [81] W. Choi, H.C. Shin, J.M. Kim, J.Y. Choi, W.S. Yoon, Modeling and applications of electrochemical impedance spectroscopy (EIS) for lithium-ion batteries, *J. Electrochem. Sci. Technol.* 11 (2020) 1–13, <https://doi.org/10.33961/JECST.2019.00528>.
- [82] C. Ho, I.D. Raistrick, R.A. Huggins, Application of A-C techniques to the study of lithium diffusion in tungsten trioxide thin films, *J. Electrochem. Soc.* 127 (1980) 343.
- [83] S.H. Yu, C.K. Park, H. Jang, C.B. Shin, W. Il Cho, Prediction of lithium diffusion coefficient and rate performance by using the discharge curves of LiFePO₄ materials, *Bull. Korean Chem. Soc.* 32 (2011) 852–856, <https://doi.org/10.5012/BKCS.2011.32.3.852>.
- [84] S. Trano, D. Versaci, M. Castellino, M. Fontana, L. Fagioli, C. Francia, F. Bella, Exploring nature-behaviour relationship of carbon black materials for potassium-ion battery electrodes, *Energy Mater.* 4 (2024) 400008, <https://doi.org/10.20517/energymater.2023.79>.
- [85] A.J. Bard, L.R. Faulkner, *Electrochemical methods: fundamentals and applications*, *Surf. Technol.* 20 (1983) 91–92.
- [86] J. Wang, J. Polleux, J. Lim, B. Dunn, Pseudocapacitive contributions to electrochemical energy storage in TiO₂ (anatase) nanoparticles, *J. Phys. Chem. C* 111 (2007) 14925–14931.
- [87] Q. Wang, Q. Liu, K. Tong, P. Guo, S. Luo, Y. Zhang, L. Qian, P. Hou, S. Yan, X. Liu, W. Mu, Recent progress of biomass-derived carbon anodes for advanced potassium-ion batteries, *Mater. Today Chem.* 51 (2026) 103299, <https://doi.org/10.1016/j.mtchem.2025.103299>.
- [88] K. Zhou, S. Wang, S. Zhang, F. Kang, B. Li, Investigating the increased-capacity mechanism of porous carbon materials in lithium-ion batteries, *J. Mater. Chem. A* 8 (2020) 14031–14042, <https://doi.org/10.1039/D0TA04054A>.
- [89] J.H. Park, H. Yoon, Y. Cho, C.Y. Yoo, Investigation of lithium ion diffusion of graphite anode by the galvanostatic intermittent titration technique, *Materials* 14 (2021) 4683, <https://doi.org/10.3390/MA14164683/S1>.
- [90] H. Wang, D. Zhai, F. Kang, Solid electrolyte interphase (SEI) in potassium ion batteries, *Energy Environ. Sci.* 13 (2020) 4583–4608, <https://doi.org/10.1039/d0ee01638a>.
- [91] L. Caracciolo, L. Madec, G. Gachot, H. Martinez, Impact of the salt anion on K metal reactivity in EC/DEC studied using GC and XPS analysis, *ACS Appl. Mater. Interfaces* 13 (2021) 57505–57513, <https://doi.org/10.1021/acsami.1c19537>.
- [92] B. Li, J. Zhao, Z. Zhang, C. Zhao, P. Sun, P. Bai, J. Yang, Z. Zhou, Y. Xu, Electrolyte-regulated solid-electrolyte interphase enables long cycle life performance in organic cathodes for potassium-ion batteries, *Adv. Funct. Mater.* 29 (2019) 1807137, <https://doi.org/10.1002/adfm.201807137>.
- [93] J. Xu, Q. Zhang, Y.-T. Cheng, High capacity silicon electrodes with Nafion as binders for lithium-ion batteries, *J. Electrochem. Soc.* 163 (2016) A401–A405, <https://doi.org/10.1149/2.0261603JES/XML>.
- [94] F. Jeschull, E. Kataev, I. Panasenko, C. Njøl, R. Félix, J. Maibach, Why half-cell samples provide limited insight into the aging mechanisms of potassium batteries, *Adv. Energy Mater.* 15 (2025) 2403811, <https://doi.org/10.1002/AENM.202403811>.
- [95] A. Hofmann, F. Müller, S. Schöner, F. Jeschull, Revealing the formation of dialkyl dioxahexane diolate products from ethylene carbonate based electrolytes on lithium and potassium surfaces, *Batteries Supercaps* 6 (2023) e202300325, <https://doi.org/10.1002/BATT.202300325>.
- [96] Y. Lei, J. Wang, D. Han, F. Yuan, H. Wang, R. Zhao, D. Huang, Y. Wu, B. Zhang, D. Zhai, F. Kang, Achieving ultralong cycle life graphite binary intercalation in intermediate-concentration ether-based electrolyte for potassium-ion batteries, *Carbon* 196 (2022) 229–235, <https://doi.org/10.1016/j.carbon.2022.04.077>.
- [97] J. Zheng, C. Hu, L. Nie, S. Zang, H. Chen, N. Chen, M. Ma, Q. Lai, Electrolyte manipulation enhanced pseudo-capacitive K-storage for TiO₂ anode, *Appl. Surf. Sci.* 611 (2023) 155617, <https://doi.org/10.1016/j.apsusc.2022.155617>.
- [98] Z. Wu, J. Zou, S. Shabanian, K. Golovin, J. Liu, The roles of electrolyte chemistry in hard carbon anode for potassium-ion batteries, *Chem. Eng. J.* 427 (2022) 130972, <https://doi.org/10.1016/j.cej.2021.130972>.
- [99] Y. Liu, C. Gao, L. Dai, Q. Deng, L. Wang, J. Luo, S. Liu, N. Hu, The features and progress of electrolyte for potassium ion batteries, *Small* 16 (2020) 2004096, <https://doi.org/10.1002/sml.202004096>.
- [100] L. Caracciolo, L. Madec, H. Martinez, XPS analysis of K-based reference compounds to allow reliable studies of solid electrolyte interphase in K-ion

- batteries, ACS Appl. Energy Mater. 4 (2021) 11693–11699, <https://doi.org/10.1021/acsaem.1c02400>.
- [101] A.K. Haridas, M.K. Sadan, H. Kim, J. Heo, S. Sik Kim, C.H. Choi, H. Young Jung, H.J. Ahn, J.H. Ahn, Realizing high-performance Li/Na-ion half/full batteries via the synergistic coupling of nano-iron sulfide and S-doped graphene, ChemSusChem 14 (2021) 1936–1947, <https://doi.org/10.1002/CSSC.202100247>.
- [102] X. Yuan, B. Zhu, J. Feng, C. Wang, X. Cai, R. Qin, Recent advance of biomass-derived carbon as anode for sustainable potassium ion battery, Chem. Eng. J. 405 (2021) 126897, <https://doi.org/10.1016/J.CEJ.2020.126897>.